Effect of reactive magnesium oxide in alkali-activated fly ash mortars exposed to accelerated CO_2 curing

David Suescum-Morales[a], Miguel Bravo[b], Rui Vasco Silva[c], José Ramón Jiménez[a*], Jose María Fernandez-Rodriguez[d], Jorge de Brito[c***]**

[a] Departamento de Ingeniería Rural, Construcción Civiles y Proyectos de Ingeniería. Escuela Politécnica Superior de Belmez, Universidad de Córdoba, Córdoba, España.

[b] CERIS, Department of Civil Engineering, Barreiro School of Technology, Polytechnic Institute of Setúbal, Lavradio, Portugal.

[c] CERIS, Department of Civil Engineering, Architecture and Georresources, Instituto Superior Técnico (IST), Universidade de Lisboa, Lisbon, Portugal.

[d] Departamento de Química Inorgánica e Ingeniería Química, Escuela Politécnica Superior de Belmez, Universidad de Córdoba, Córdoba, España.

[*]Corresponding authors at: Departamento de Ingeniería Rural, Universidad de Córdoba, Ed. Leonardo Da Vinci, Campus de Rabanales, Ctra. N-IV, km-396, CP 14014 Córdoba, Spain (José Ramón Jiménez). **Departamento de Química Inorgánica e Ingeniería Química, Instituto Universitario de Nanoquímica (IUNAN), Facultad de Ciencias, Universidad de Córdoba, Campus de Rabanales, Edificio Marie Curie, E-14071, Córdoba, Spain (José María Fernández-Rodríguez). [***]CERIS, Department of Civil Engineering, Architecture and Georresources, Instituto Superior Técnico (IST), Universidade de Lisboa, Lisbon, Portugal

E-mail addresses: um1feroj@uco.es (J.M. Fernández-Rodríguez), jrjimenez@uco.es (J.R. Jiménez), jb@civil.ist.utl.pt (J. de Brito)

Abstract

The effect of reactive magnesium oxide (MgO) as partial fly ash replacement in alkali-activated fly ash mortars (0, 10 and 20 %) was studied under two different environments: conventional climatic chamber and climatic carbonation chamber with 0.04 and 5 % level of CO_2 respectively. A complete characterisation of all raw materials was performed. The effect of replacing fly ash with MgO resulted in a decline of compressive and flexural strength, ultrasonic pulse velocity and dynamic Young's modulus mainly due to the formation of weak and expansive brucite, detected by X-ray diffraction (XRD). Carbonation depth and shrinkage also were obtained. CO_2 curing improved the physicomechanical properties, due to the formation of nesquehonite in samples with MgO. An improvement of CO_2 absorption of 2 g CO_2/kg mixes with the CO_2 curing and the substitution of fly ash with MgO was obtained (determined by thermogravimetric and differential thermal analysis).

Keywords: Alkali-activated cement; Fly Ash; Mortar; Accelerated carbonation; Carbon capture; Microstructure, Reactive MgO

Graphical Abstract

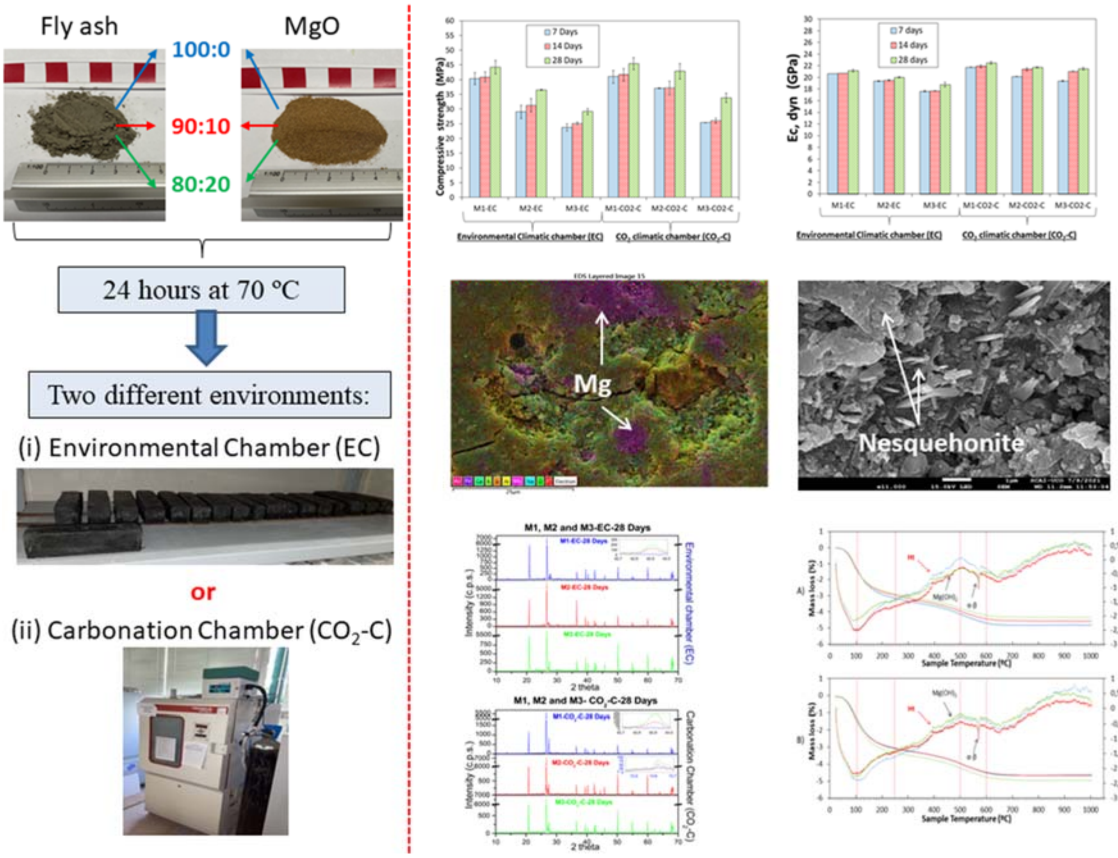

1 Introduction

Emissions of carbon dioxide (CO_2) into the atmosphere have significantly increased in recent years (33.1 Gt in 2018), reaching levels of approximately 470 ppm today, leading to global warming [1–3]. The cement industry produces approximately 5-7% of global CO_2 emissions; around 900 kg of CO_2 is emitted to the atmosphere for producing one ton of cement [4,5]. Furthermore, approximately 50-60% of ordinary Portland cement (OPC) production-related CO_2 emissions are released from the calcination (decarbonation) of limestone (Eq. (1)) [6,7]. Naturally, it is not possible to decrease this amount by improving the process' energy efficiency and thus it is essential to look for new solutions that reduce the use of OPC [5,8–11].

$$CaCO_3 \rightarrow CO_2 + CaO \qquad (1)$$

Alkali-activated materials (AAM) are being developed as an alternative to reduce the use of OPC [8,10,12–17]. These materials are presented as a component of the current and future suite of "sustainable cementing binder systems" [18]. These binders can be produced from a wide range of aluminosilicate precursors from several industrial processes: fly ash (FA), silica fume, rice husk ash, sugarcane bagasse ash, and ground granulated blast furnace slag (GGBFS), among others [8,10,19–23]. Sodium hydroxide (NaOH), potassium hydroxide (KOH), sodium silicate (Na_2SiO_3) or their combination have been used as activators [24]. The process involves the dissolution of a solid aluminosilicate (precursors) under alkaline conditions (alkaline activator) under surface hydration of the particles of the precursors followed by coagulation, gelation and polycondensation to form a gel and subsequently a hardened inorganic polymer structure [9,25–27]. The following reactions occur during the polymerization (Eqs. 2-3) [28–30]:

$$(Si_2O_5Al_2O_2)_n + H_2O + OH^- \rightarrow Si(OH)_4 + Al(OH)^{4-} \qquad (2)$$

$$Si(OH)_4 + Al(OH)^{4-} \rightarrow (Si - O - Al - O)_n + 4H_2O \qquad (3)$$

FA and GGBFS have been considered as the main precursors for AAM products and there is a lot of research with these precursors [5,8,15,24,29,31–35] even in engineering applications [36–38]. However, the use of renewable energy sources for energy production [39] and the preference of electric arc furnaces over blast furnaces due to their higher efficiency in recycling ferrous metals [5] have led to a withering production of FA and GGBFS, respectively [40]. Therefore, the study of new precursors is warranted to guarantee the viability of future AAM production.

In recent years, MgO has been identified as one of the important parameters of AAM since it affects physicochemical changes and microstructural growth [41]. MgO, when used as an addition in GGBFS-based AAMs, has been found to reduce shrinkage due to the formation of $Mg(OH)_2$ gel or hydrotalcite-like phases [42] and to improve the mechanical performance [43,44]. Ahmad et al. [24] studied the substitution of FA and GGBFS used in conjunction with different percentages of MgO revealed a significant improvement in long term compressive strength and water absorption performance. Vo et al. [45] studied the simultaneously effect of the use of high rice husk ash and MgO to modified alkali-activated slag, caused a negative effect on the workability but improved the mechanical properties and thermal conductivity. Ke and Duan [46] checked a composition-strength model (Gaussian processes, GP) predicted a 3 % optimum Mg content for maximum mechanical performance. Jin [43,44] reported that MgO accelerated early hydration and significantly reducing the drying shrinkage. The main effect of MgO in AAM is related to the densification of the microstructure since it increases the reaction rate and increases the total amount of reaction products [47–52]. The literature review has shown no studies on relatively high MgO content (> 10%) as FA replacement in alkali-activated mortars without GGBFS.

The carbonation of reinforced CBM is considered a pathology since it results in the corrosion of the reinforcement. However, carbonation can be beneficial for non-reinforced CBM as it favours CO_2 capture and enhanced mechanical performance. The idea of capturing CO_2 through accelerated carbonation is not new in CBM [53] and there have been many studies investigating the effect of an extensively carbonated matrix. This process increases $CaCO_3$ content, improves mechanical properties, increases density, decreases the porosity, as may translate in reduced curing time [2,3,54–63]. Although the carbonation mechanism in AAM is not yet fully understood, it is expected to be different from that of CBM due to the existence of different mineralogical phases [64]. Some authors indicate that AAM have a low resistance to carbonation, so its use in structural elements can lead to a catastrophic result due to the depassivation of the reinforcement [65,66]. However other authors indicated that AAM have a fairly acceptable level of resistance to carbonation [67–69]. According to Bernal et al [70], these different points of view are due to: (i) the different exposure conditions (CO_2 level); (ii) few studies examining the carbonation of these materials and (iii) the lack of specific standards (in the case of CBM, EN 13295 [71] is used). Usually the measure of "carbonation" is merely decline in pH and not that the material presented higher levels of CO_2 uptake. The method itself is at fault. Carbonation studies on AAM can fill this knowledge gap and clarify such questions.

Alkaline activation of high magnesium slag under accelerated carbonation allows a layered double hydroxide (LDH), which is identified as a hydrotalcite-like phase [72–75]. Hydrotalcites are brucite-like layered materials with hydroxide groups on their surface [76]. Between the layers of hydrotalcite there are interlayer anions, such as carbonates [77]. It has already been shown that hydrotalcite can react and capture CO_2 [1,3,55]. Bernal et al. [74] showed that as the content of MgO increases in alkaline slag activation, the depth of carbonation decreased, which is attributed to the greater formation of LDH [78]. MgO has a high capacity to sequester significant amounts of CO_2 [79]. Therefore, the substitution of fly ash by MgO in alkaline-activated mortars and the curing in CO_2 atmosphere could increase the carbon capture capacity of these materials. There are no studies that calculate the amount of CO_2 fixed by alkali-activated fly ash mortar with different percentages of FA substitution by MgO under accelerated carbonation. This research covers this lack of information.

This research aims to study the effect of reactive magnesium oxide in alkali-activated fly ash mortars cured in a CO_2-rich environment. Two main variables were investigated: (i) fly ash substitution by MgO and (ii) type of curing regime (i.e. normal climatic chamber or accelerated carbonation chamber). This study can be divided in two sections: (a) characterisation of the raw materials and (b) characterisation of three types of alkali-activated fly ash mortars with 0, 10 and 20 % of substitution fly ash by MgO. In the first section were used X-ray fluorescence (XRF), X-ray diffraction (XRD), grain size distribution and thermogravimetric and differential thermal analysis (TGA/DTA). For the second section, in first place the "macro-behaviour" was studied: compressive and flexural strength, ultrasonic pulse velocity (UPV), dynamic Young's modulus, dry bulk density, accessible porosity for water, shrinkage and depth of carbonation. After this, the "macro-behaviour" was explained through "micro-behaviour" with: XRD, TGA/DTA, Scanning electron microscopy (SEM), energy dispersive X-ray spectroscopy (EDS) and backscattered electron (BSE). Also the CO_2 captured by the different mixtures was calculated with TGA/DTA. No research has been found that studies the effect of reactive magnesium oxide in alkali-activated fly ash mortars cured in a CO_2-rich environment.

2 Materials and methods

2.1 Materials

Class F coal fly ash (FA) [80], provided by EDP - Gestão da Produção de Energia, S.A. at the Sines Power Plant, was used as the primary binder (skeletal density of 2431 kg/m^3). The reactive MgO was supplied by Magnesitas de Rubian (skeletal density of 3400 kg/m^3), a Spain Company. The total amount of MgO according to the manufacturer is 83 %. The aggregates were composed of fine (0/1 mm) and coarse (0/4 mm) siliceous sand (FS and CS, respectively) with a skeletal density of 2637 and 2617 kg/m^3, respectively, and water absorption of 0.4% and 0.5%, respectively. A Na_2SiO_3 solution (1370 kg/m^3) and reactive grade sodium hydroxide pellets (2130 kg/m^3) were used as alkaline activators. The Na_2SiO_3 solution was comprised of 28% SiO_2, 8% Na_2O and 64% H_2O by weight. Tap water used in the preparation of the alkaline activator corresponds to that from the public network of EPAL company, complying with Directive 98/83/CE. A Sikaplast-717 water reducing admixture was used, consisting of a combination of synthetic organic naphthalene-based dispersants, with a density of 1.21 ± 0.03 kg/dm^3 and a pH of 10 ± 1.

2.2 Mix design and curing conditions

The mix design followed a similar approach to that proposed in other studies [5,81]. All mixes presented a mass ratio precursor/aggregate of 1/3, a water/precursor ratio of 0.4, and a superplasticizer/precursor ratio of 0.002. The total amount of precursor was 450 kg/m^3. A Na_2O/precursor ratio of 14% was used. The SiO_2/Na_2O ratio by mass was 1. Three types of mixes were studied: 100% FA (M0 or reference); 90% FA + 10% MgO (M10); and 80% FA + 20% MgO (M20).

The production of all samples with a standard size of 40 × 40 × 160 mm was carried out as per EN 196-1 [82], adapted for alkali-activated mortars. The Na_2SiO_3 solution, NaOH and water were mixed 24 hours before mortar production to avoid polymerisation catalysis due to the activator's exothermic nature. The moulds containing the specimens were wrapped in plastic film and subsequently cured for 24 hours at 70 ºC. After that, the samples were demoulded and cured in two different environments (i.e. normal climatic chamber or carbonation chamber) and tested at three ages (i.e. 7, 14 and 28 days). The conditions of each environment are the following:

(a) Environmental chamber (EC) - CO_2 level equivalent to atmospheric concentration (≈0.04%), at 20 ºC and 60%RH.
(b) Carbonation chamber (CC): Heraeus Vötsch HPS 500 with 5% CO_2 (supplied by Linde and with 99.995% purity), 20 ºC and 60%RH.

A summary of the quantities used for each mix and specimen coded used are shown in Table . Fig.1 shows a summary of the sample preparation process (a and b) and different environments (c).

Table 1 - Mortar mixes composition (kg/m^3) and specimen code

Mortar type	FA	MgO	NaOH	Water	Na_2SiO_3	FS	CS	Superplasticizer
M0	450	-	57	42	224	436	1010	0.9
M10	405	45	57	42	224	436	1010	0.9
M20	360	90	57	42	224	436	1010	0.9

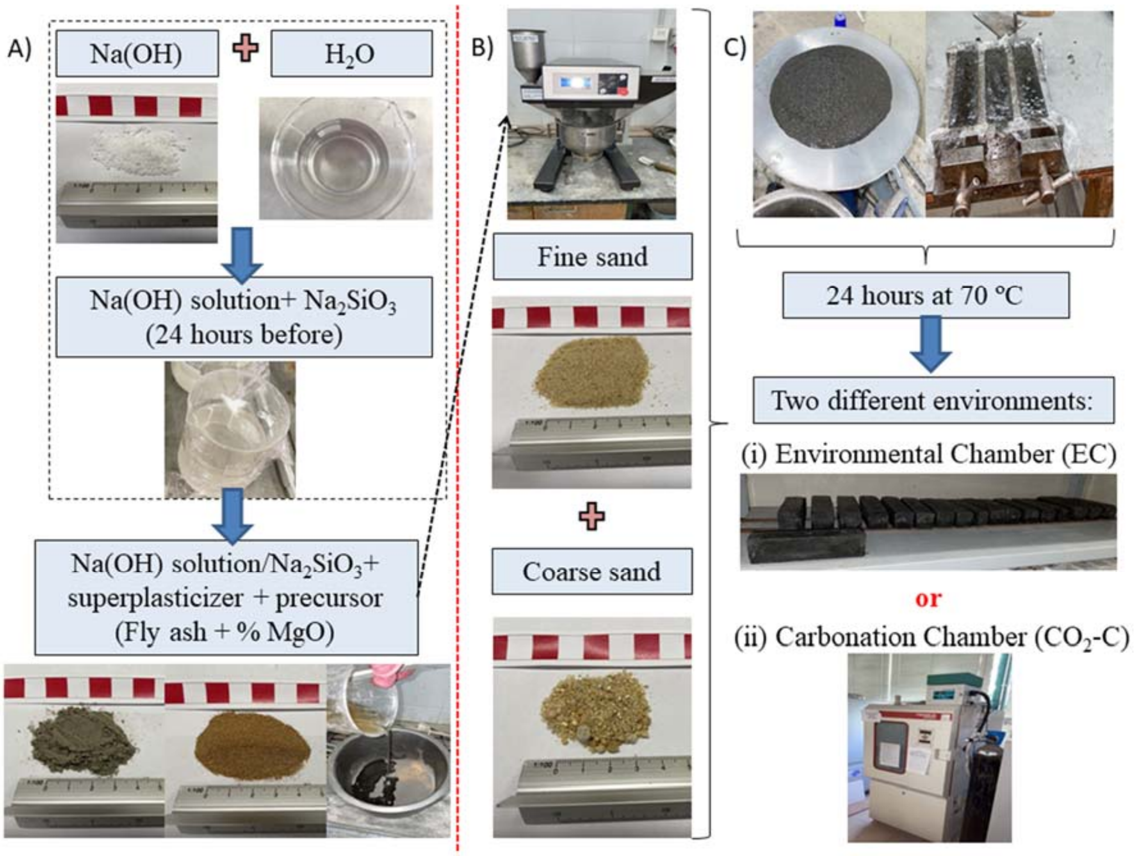

Figure 1 - Summary of the sample preparation process (A) and (B); (B) two different curing environments

2.1 Test methods

2.1.1 X-ray fluorescence spectrometry analysis

The chemical composition of the solid raw materials was evaluated using a non-corrosive wavelength dispersive X-ray fluorescence spectrometry analysis (XRF), using a ZSX PRIMUS IV (Rigaku) equipment with a power of 4 kW.

2.1.2 **X-ray diffraction analysis**

The solid raw materials and hardened mixes (M0, M10 and M20 at the ages of 7, 14 and 28 days) were characterized via X-ray diffraction (XRD) using a Bruker D8 Discover A25 instrument with Cukα (λ=1.54050 A, 40 kV and 30 mA). Diffraction patterns were obtained with a goniometric scan from 10º to 70º (2θ) at the speed of 0.016 $2\theta\cdot s^{-1}$. The hardened samples were first powdered and quartered. The diffractogram peaks of the crystalline phases were compared with those of the JCPDS library [83].

2.1.3 **Particle size distribution**

The particle size distributions of the precursors were in a Mastersizer S. Analyser (Malvern Instruments) using ethanol as a dispersant. All samples were sonicated for 10 min before the analysis. The results are shown as the average of three repetitions.

2.1.4 **Thermogravimetric analysis and differential thermal analysis**

Thermogravimetric analysis (TGA) and differential thermal analysis (DTA) were conducted for the solid raw materials and hardened mixes (M0, M10 and M20 at the ages of 7, 14 and 28 days). TGA/DTA was carried out in a Setaram Setys Evolution 16/18 apparatus, using alumina crucibles under airflow and argon. The heating rate was $5°\cdot min^{-1}$ and the temperature range was approximately 20–1000 °C. The results are shown as the average of two repetitions.

2.1.5 **Scanning electron microscopy**

The morphology and composition of the precursors were obtained using scanning electron microscopy (SEM), energy-dispersive X-ray spectroscopy (EDS) and backscattered electron (BSE) imaging with a JEOL JSM 7800 F. No sputtering was used. Small samples of M0 and M20 (2 × 2 × 2 cm), cured in both environments for 28 days, were placed in epoxy resin (3 cm in diameter) and polished with silicon carbide papers after 48 h. To obtain maximum quality, a gold sputtering was used.

2.1.6 **Fresh and physical-mechanical properties**

The fresh density of the mixes was evaluated according to EN 1015-6 [84]. The consistence of fresh mortars was tested following EN 1015-3 [85]. The flexural and compressive strengths of hardened mixes were tested in accordance with EN 1015-11 [86] after 7, 14 and 28 days for each of the curing environments (EC and CC). Ultrasonic pulse velocity (UPV) was measured for these same samples in accordance with EN 12504-4 [87]. The dynamic Young's modulus was also measured [88]. The drying shrinkage was measured according to EN-1015-13 [89] and the dry bulk density was determined according to EN 1015-10 [90]. The carbonation depth was measured by spraying a freshly split surface with phenolphthalein solution (1 g phenolphthalein, 30 ml demineralized water and 70 mL ethanol) [71].

3 **Results and discussions**

3.1 **Raw materials**

Table 2 shows the chemical composition of FA, FS, CS and MgO. For FA, the majority of oxides were SiO_2, Al_2O_3, and CaO. These components play the most important role during the alkaline activation of industrial aluminosilicate wastes [22]. For FS and CS, SiO_2 was the largest oxide due to the siliceous nature of the natural aggregates. A higher purity, due to the higher SiO_2 content was shown in CS. For MgO, the total amount of MgO was exactly as marked by the manufacturer (83%). Also SiO_2, CaO, Fe_2O_3 and Al_2O_3 were found in smaller amounts. He et al [42] found the same value for MgO (83.09).

Table 2. XRF chemical composition of the raw materials

Oxides	FA	FS	CS	MgO
Na_2O	1.2	0.9	0.1	0.2
MgO	1.8	0.1	0.04	83
Al_2O_3	24.4	7	3.9	2.1
SiO_2	57.5	87.1	92.8	8
P_2O_5	0.4	0.04	0.04	0.2

SO_3	0.8	-	-	0.1
Cl_2O_3	-	-	-	0.02
K_2O	2.7	4.0	2.35	0.2
CaO	7.1	0.2	0.2	3.4
TiO_2	1	0.1	0.07	-
MnO_2	0.1	-	-	0.1
Fe_2O_3	2.6	0.4	0.5	3.3
CuO	0.01	-	-	-
ZnO	0.03	-	-	-
SrO	0.09	-	-	-
ZrO_2	0.01	-	-	-
BaO	0.2	-	-	-
Cr_2O_3	0.03	-	-	-

The XRD spectra for FA, FS, CS, MgO and NaOH are shown in Figure . The main crystalline phase of FA was quartz (SiO_2) (05-0490) [83]. Other minor phases were also identified: mullite ($3Al_2O_3 \cdot 2SiO_2$) (02-0431) [83], calcite ($CaCO_3$) (05-0586) [83] and marwinite ($Ca_3Mg(SiO_4)_2$) (35-0591) [83]. The same phases were found by several authors [30,91]. Amorphous content was found between 15 and 40 2 theta. As expected, the main crystalline phase of FS was quartz (05-0490) [83]. Albite ($NaAlSi_3O_8$) (89-6426) [83] and orthoclase ($KAlSi_3O_8$) (75-1592) [83] - were also found. For CS, the same phases were found, except for albite. The higher purity of CS versus FS in XRF has already been discussed. Exactly the same observation with sands of similar size was found by Suescum-Morales et al [92]. The main phase of MgO was periclase (04-0829) [83], but there were also other peaks for calcite (05-0586) [83], talc ($Mg_3Si_4O_{10}(OH)_2$) (10-0386) [83] and dolomite ($CaMg(CO_3)_2$) (11-0078) [83]. The same phases were found by Gonçalves et al [93].

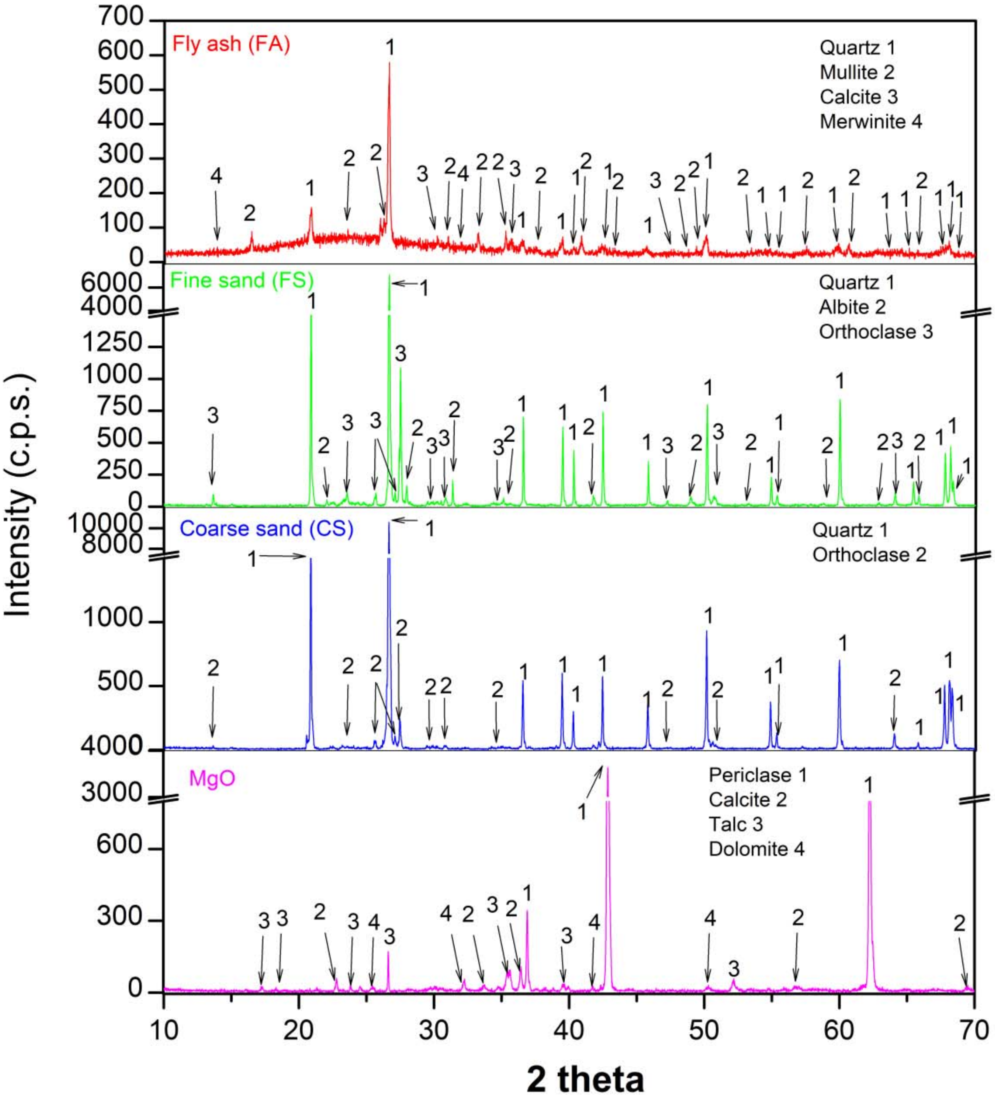

Figure 2 - XRD patterns for fly ash (FA), fine sand (FS), coarse sand (CS) and MgO

Figure shows the particle size distribution for FA and MgO. The highest peak corresponded to 9.7 µm. FA presented the largest distribution peak. FA presented the largest distribution peak at around 20 µm and the smaller and wider peak at around 0.35 µm, indicating an adequate amount of very fine particles (category N) [94]. MgO showed that most of its particles had a particle size distribution at around 158 µm. Smaller particles between 0.1 µm and 1 µm were also identified.

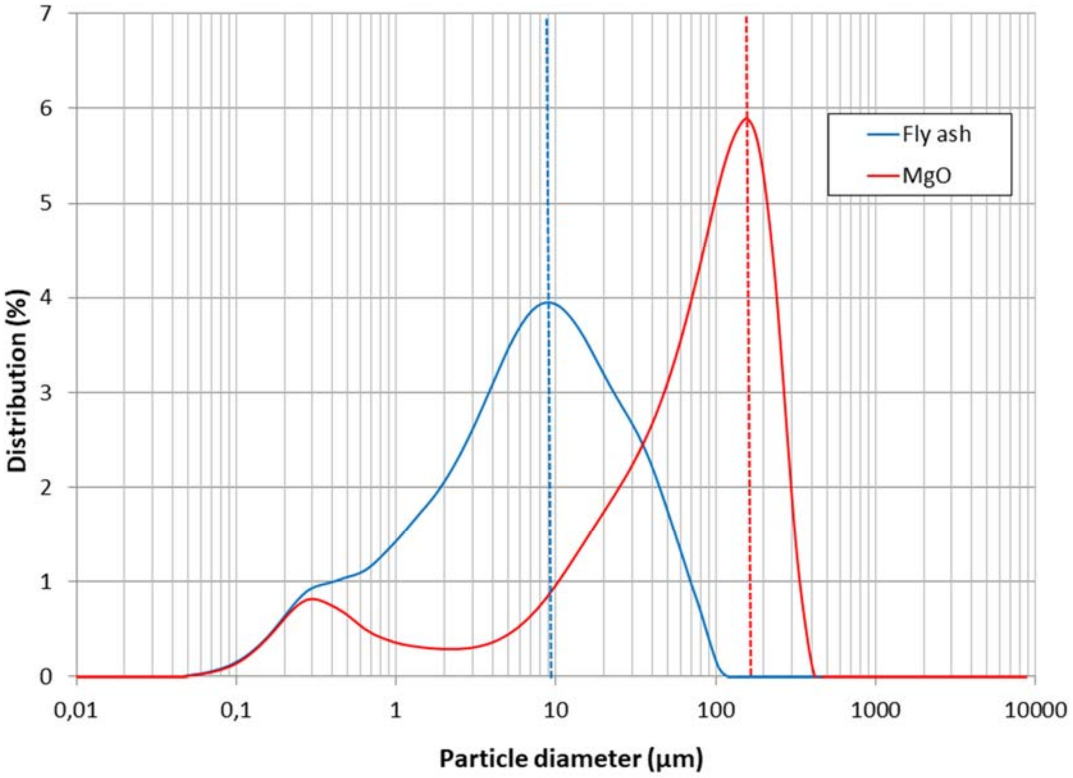

Figure 3 - The particle size distributions of FA and MgO

Figure shows the TGA/DTA for FA, FS, CS and MgO. The TGA curve of FA shows a gradual slight mass loss from 105 ºC to 450 ºC most likely due to the presence of moisture. A major mass loss was observed from 450 ºC to 730 ºC, attributed to oxidation and combustion of unburnt coal. A small amount of it was also due to the decarbonation of calcite (Figure). From 730 to 1000 ºC the weight loss was negligible. The same stages and observations were obtained by Haq et al [95]. For FS, a slight weight loss (0.07%) was observed, likely due to the presence of the albite, which was detected in XRD (Figure). For CS no weight loss was observed. An endothermic peak was detected around 570 ºC for FS and CS corresponding to the transformation in the crystal structure of the sand of the phase from quartz α to β [96]. Around 710 ºC another common endothermic peak for both types of sand was observed. This could be attributed to the formation of siloxane bridges from the dehydroxylation of silanol groups on the internal surface of the sand samples [97]. A similar results were observed by others [92,97,98]. A significant mass loss was observed for MgO at temperatures between 300 ºC and 500 ºC, indicating dehydroxylation of $Mg(OH)_2$, which suggests partial hydration of the addition [79]. An important mass loss was observed at about 640 ºC probably due to the decarbonation of calcite and dolomite (Fig. 2).

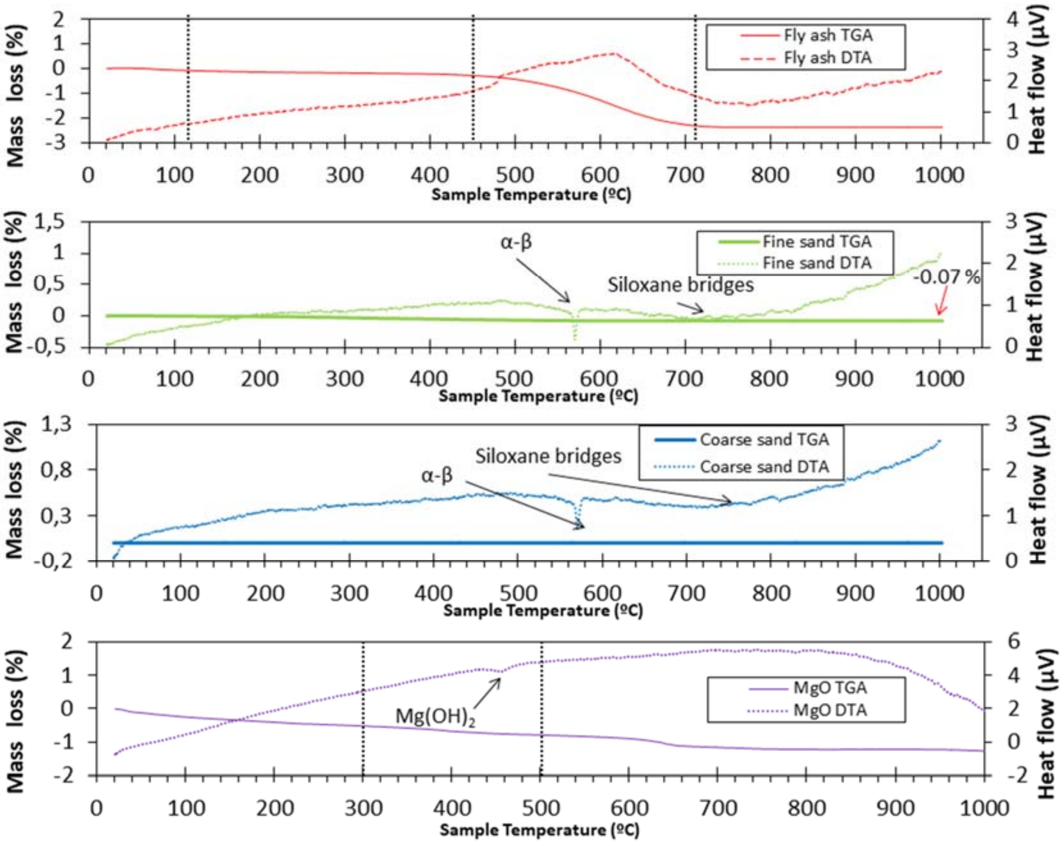

Figure 4 - TGA (solid lines) and DTA (dotted lines) for FA, FS, CS and MgO

Figure shows SEM micrographs of FA (A) and MgO (B). The spherical structure is the predominant shape in FA. At higher magnification, it can be seen that most of the spheres have a diameter of ~10 µm, which is in agreement with the findings of the particle size distribution analysis (Figure). There are also unshaped fragments. The EDS mapping indicated that the main elements were Si, Al and Ca (Fe, Mg, Ti, K and Na among others were also found). This is in agreement with the XRF and XRD results. MgO particles show a typical irregular shape [45,99]. The EDS mapping indicated that the main elements were Mg, Si and Ca (Fe and Al among others).

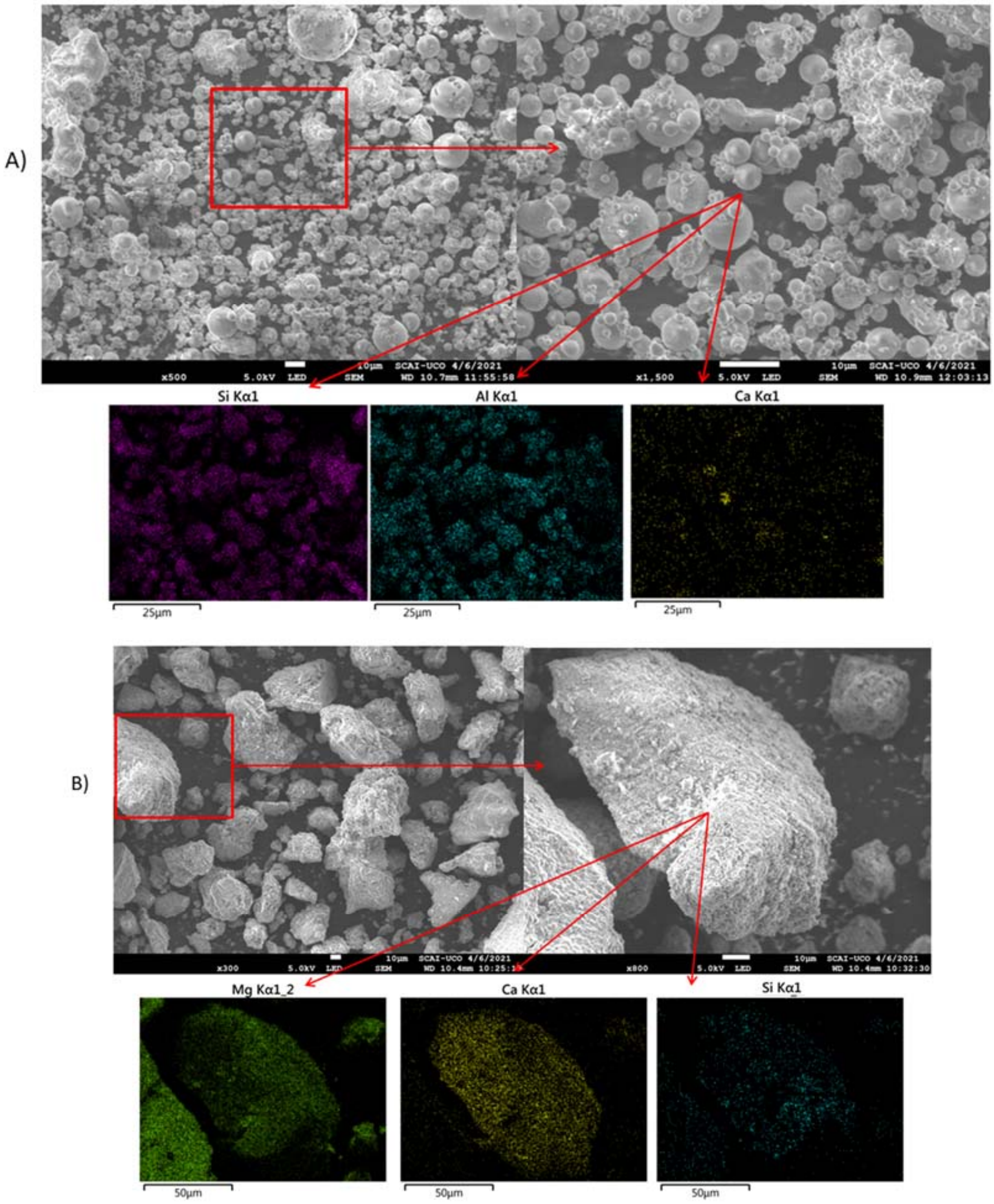

Figure 5 - SEM images and EDS mapping for (A) FA and (B) MgO

3.2 Consistence and bulk density of fresh mortars

Consistence decreased as the MgO content increased (M0>M10>M20, see Figure), and previously witnessed by others [42,45,52]. This is most likely due to the irregular shape of MgO particles versus the sphericity of FA (Figure), which causes greater interparticle friction. Nevertheless, Ahmad et al. [24] obtained the opposite, as the MgO content increased, consistence increased. This higher consistence was associated with the rounded shape of the MgO particles used and the balling effect of round particles. This highlights the importance of studying the microstructure of the MgO used. The fresh density increased with the MgO content (M0<M10<M20, see Figure), which is justified by the higher skeletal density of MgO (3400 kg/m^3) with respect to that FA (2431 kg/m^3).

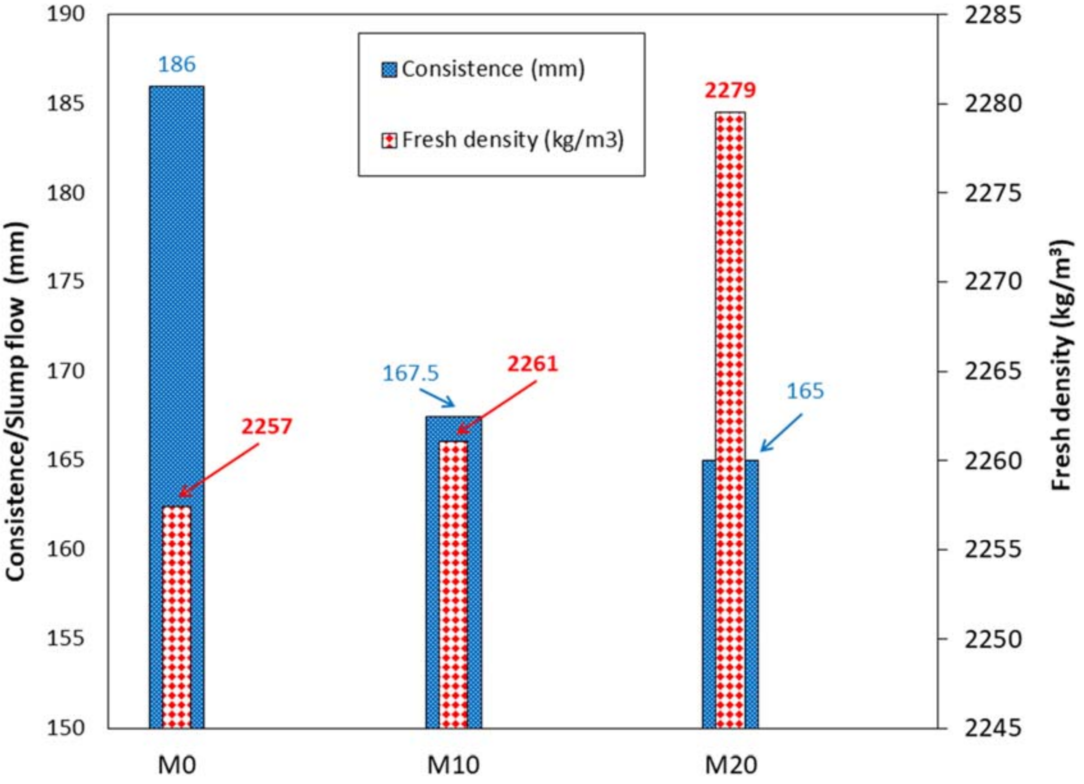

Figure 6 - Consistence and fresh density

3.3 Compressive and flexural strength

The compressive strength development of M0, M10 and M20, under EC and CC at the ages of 7, 14 and 28 days, is shown in Figure . Despite the small development between 7 and 14 days, the compressive strength increased over time in all samples. After 7 days in an EC, the effect of replacing 10% and 20% FA with MgO resulted in compressive strength decreases of 39.1% and 69.7%, respectively (M0-EC-7 Days vs. M10 and M20-EC-7 Days). These differences lessened with increasing curing age, with decreases of 21.2% and 52.3%, respectively, after 28 days. The decline in compressive strength may be due to the formation of excessive hydrotalcite and brucite, which affects the specimens' volumetric stability due to expansive reaction products

[42]. Performance decline has been observed by others studying increasing MgO content mainly due to the formation of mainly hydrotalcite [42,44,75]. Brucite ($Mg(OH)_2$), formation according to Eq. (4), is known to have a weak structure [79,93].

$$MgO + H_2O \rightarrow Mg^{2+} + 2OH^- \rightarrow Mg(OH)_2 \qquad (4)$$

Exposing the samples to CO_2 led to enhanced performance, except for the reference mortar, wherein the mean values remain comparable for both curing environments (EC vs. CC).Among other possible causes, this result could be related to the formation of insoluble calcium carbonate ($CaCO_3$) and the consequent densifying of the mortar microstructure, which can also occur in fly ash systems activated by calcium-rich alkalis [8,100–102]. Curing in CO_2 with respect to a normal curing environment of the samples that replacing 10% FA with MgO (M10-EC vs. M10-CO_2-C) showed increases of 27.6, 18.7 and 17.3 % for the ages of 7, 14 and 28 days, respectively. The substitution of 20% FA by MgO and curing in CO_2 showed increases compared to normal curing (M20-EC vs. M20-CC) of 6.7%, 3.9% and 15.8% for the ages of 7, 14 and 28 days respectively. This shows that carbonation of mixtures with MgO improves the compressive strength. This may be due to the brucite reacting with the CO_2 from the curing process leading to the formation of hydrated magnesium carbonates (HMCs), mainly nesquehonite ($MgCO_3 \cdot 3H_2O$), with a dense formation and needle-like morphology, allowing for improved strength [79].

The flexural strength development of M0, M10 and M20 under EC and CC at the ages of 7, 14 and 28 days is shown in Figure . A similar trend to that for compressive strength was observed. The effect of replacing 10% and 20% FA with MgO resulted in flexural strength decreases. The high flexural strength values obtained, compared to what would occur in a conventional cement mix, are striking. One of the possible reactions to this result, would be the three-dimensional structure as a result of the polymerization reactions providing physical strength [103].

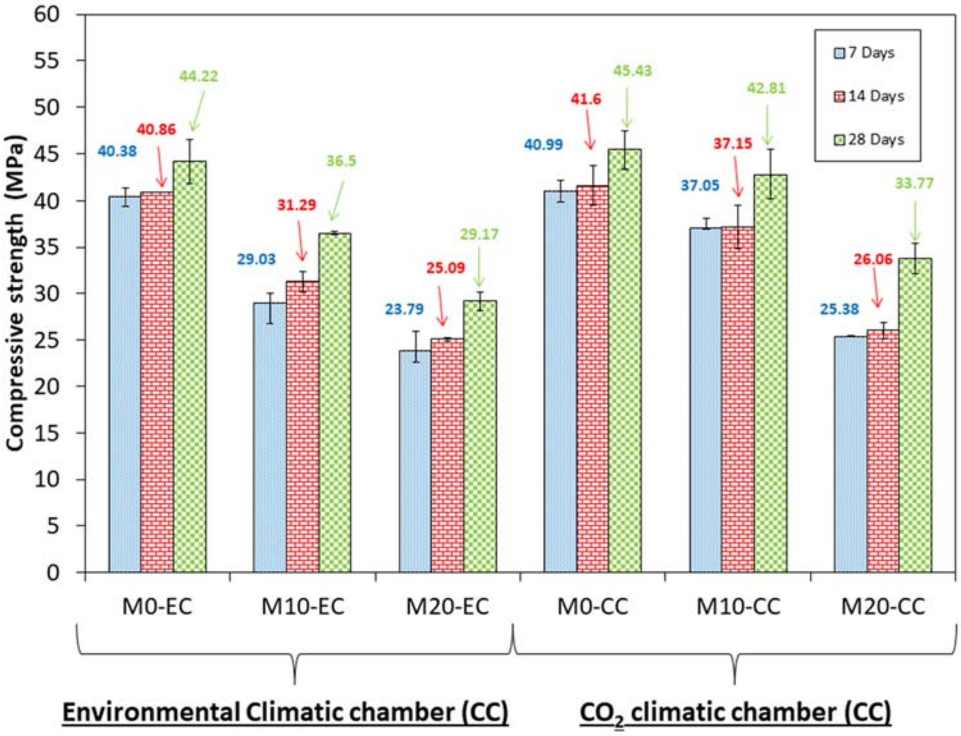

Figure 7 - Compressive strength development of M0, M10 and M20 under EC and CC at the ages of 7, 14 and 28 days

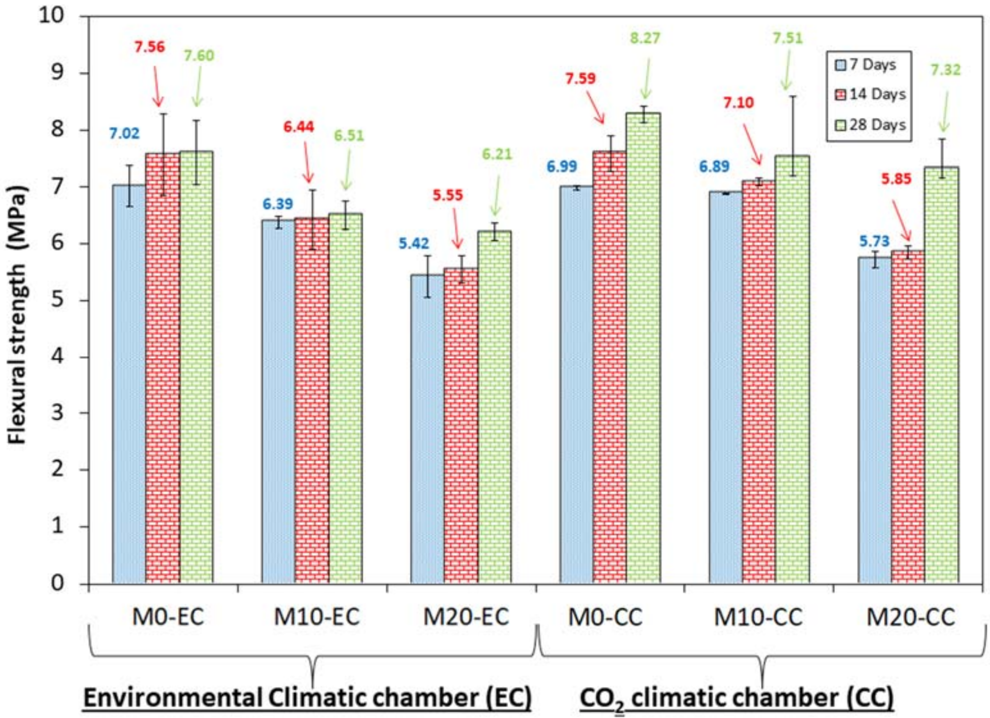

Figure 8 - Flexural strength development of M0, M10 and M20 under EC and CC at the ages of 7, 14 and 28 days

3.4 Ultrasonic pulse velocity and dynamic Young’s modulus

The ultrasonic pulse velocity (UPV) test (Figure) of M0, M10 and M20 under EC and CC at the ages of 7, 14 and 28 days is based on the pulse velocity method to provide information concerning the uniformity, cavities, cracks, and defects of the samples. The UPV values are consistent with the compressive strength results. The pulse velocity increased with increasing sample age. However, this increase was very small or almost non-existent between the age of 7 and 14 days, yet high between 14 days and 28 days. It is possible that, aside from the initial catalysis prompted by the thermal curing stage, the ongoing dissolution and polymerization reaction may have been more relevant during this period. Additional evaluation is needed to ascertain this. Furthermore, the UPV values obtained from the reference mixture (M0-EC) were similar to those obtained by other authors [5,104]. Again, as observed with the compressive and flexural strength values, the effect of replacing FA with MgO decreased the UPV of mixes cured in the EC.

Curing in CO_2 increased the UPV values in all samples studied, which may be related to the aforementioned densification of the microstructure ($CaCO_3$) [100,101]. The smallest increase occurred for the reference mixture at the age of 7 and 14 days (M0-EC vs. M0-CC). The mixes with MgO cured in CO_2 showed a higher increase in the UPV values than the reference sample (M10 and M20-EC vs. M10 and M20-CC). This may be related to the formation of the dense nesquehonite [79]. According to the International Atomic Energy Agency (IAEA) [105], the quality of all the alkali-activated mortars studied under CO_2-C can be classified as “good” quality (3500-4500 m/s).

The results of the dynamic Young’s modulus are presented in Figure . The trend agrees with the findings for compressive strength, flexural strength and UPV. The values found for the reference mixture (M1-EC) were similar to those found by several authors [5,106]. Replacing FA with MgO resulted in a slight decrease of the dynamic Young’s modulus. This decline is likely due to the lower compatibility of MgO with conventional AAM precursors (i.e. low amorphous aluminosilicate phases) and thus the formation of a lower amount of strength-giving phases (i.e. C-(N)-A-S-H). Naturally, the lower interconnectivity of the microstructure and more empty spaces led to a decline in the dynamic Young's modulus.

As expected, curing in CO_2 increased the dynamic Young's modulus. This increase was more relevant for the samples containing MgO than for the reference sample, which could be related to the formation of the dense nesquehonite [79].

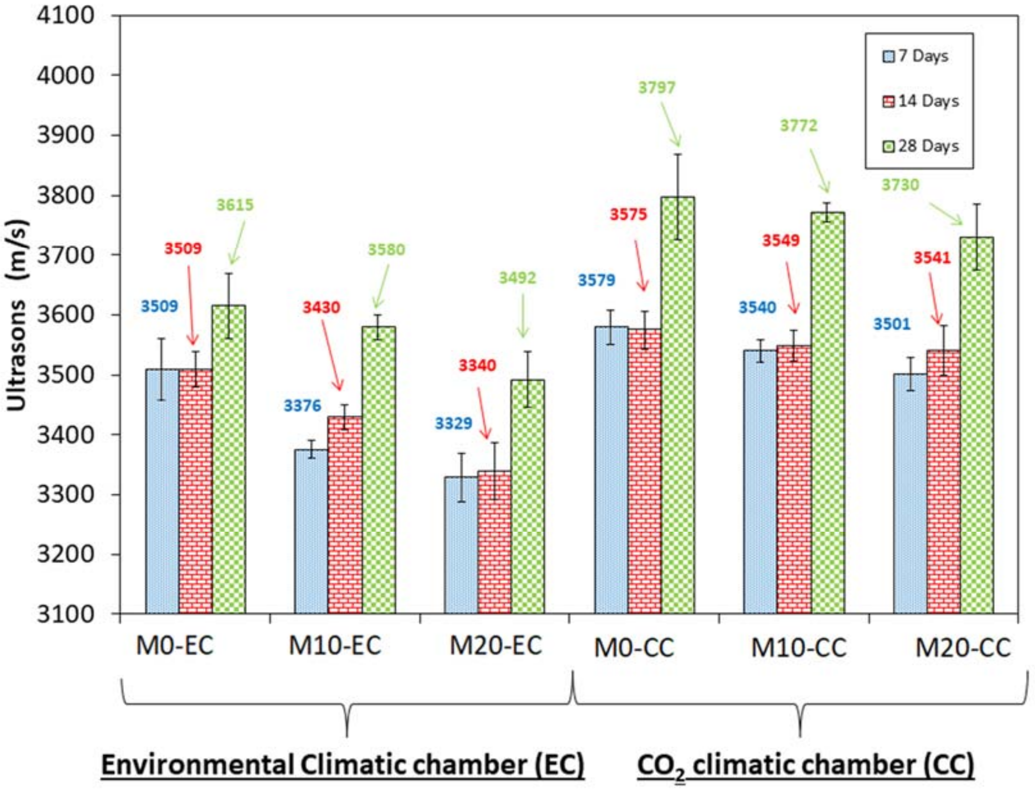

Figure 9 - Ultrasonic pulse velocity (UPV) of M0, M10 and M20 under EC and CC at the ages of 7, 14 and 28 days

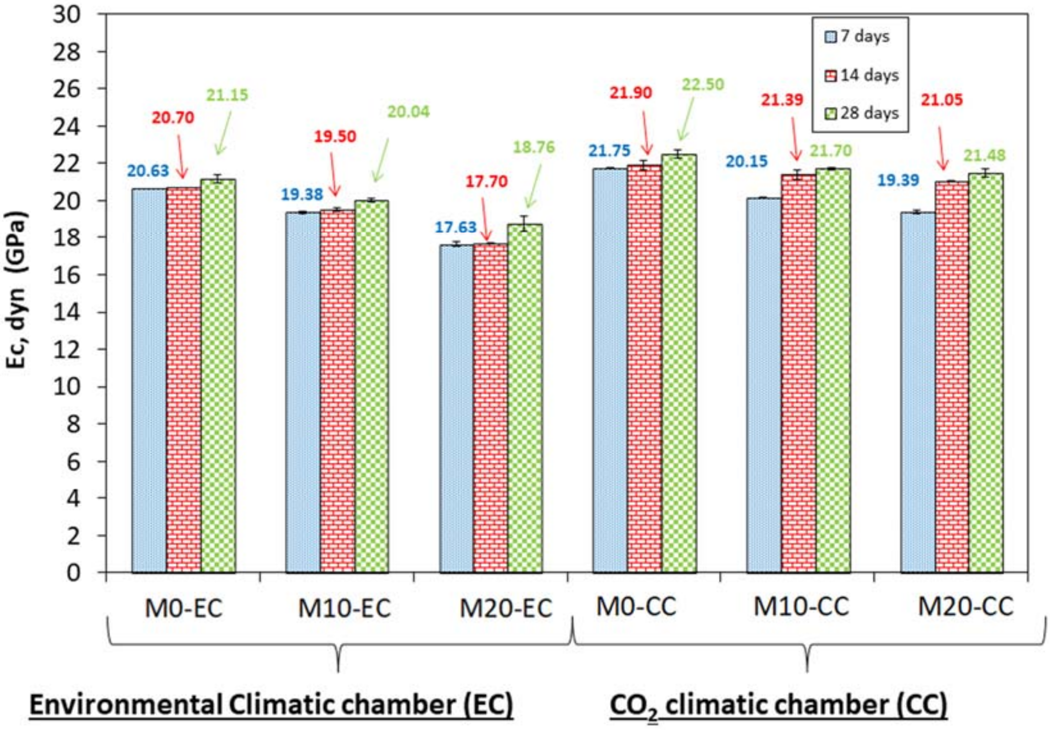

Figure 10 - Dynamic Young's modulus of M0, M10 and M20 under EC and CC at the ages of 7, 14 and 28 days

3.5 Shrinkage

Figure shows the results of the shrinkage test of M0, M10 and M20 under EC and CC at the ages of 7, 14 and 28 days. As expected, for mixes cured in an EC, the shrinkage decreased for all curing age with increasing MgO content, especially at 28 days. This is due to the formation of expansive hydration products such as brucite (Eq. 4). Some researchers indicate that this expansion is more likely due to the formation of hydrotalcite, which is more voluminous than C-S-H gel, since they did not find brucite in their studies [48,107]. This occurs in both AAM [42,108,109] and CBM [93]. Although this is phenomenon is unwanted for more stable microstructures, when it occurs in early ages, it offsets part of the deformation due to shrinkage.

Curing in CO_2 resulted in further shrinkage decrease in all samples. The smallest decrease occurred for the reference mixture, for all the curing ages studied (M1-EC vs. M1-CO_2-C). This result could be related to the formation of calcium carbonate ($CaCO_3$, densifying the microstructure) [110]. Also, when the dynamic Young's modulus is higher, the shrinkage is lower. M20-CC (20% MgO) presented an early age expansion at the age of 7 days. This may be due to the brucite reacting with the CO_2 from the curing process, leading to the formation of a dense nesquehonite.

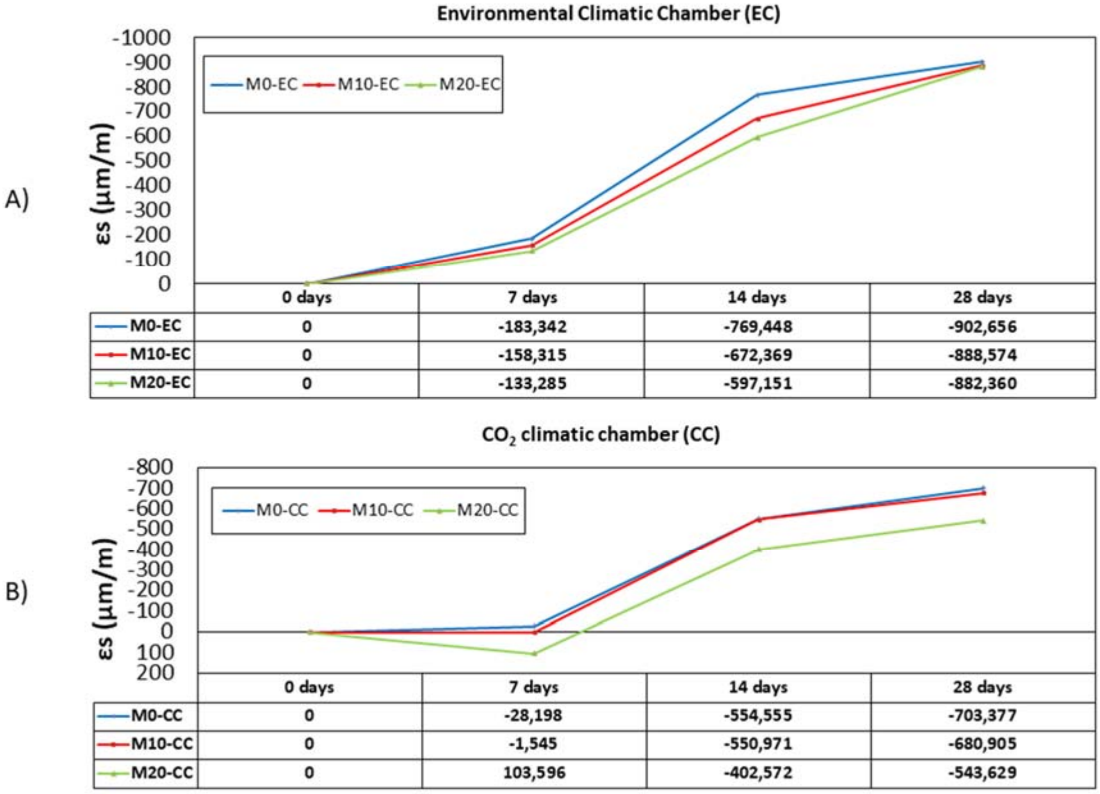

	0 days	7 days	14 days	28 days
M0-EC	0	-183,342	-769,448	-902,656
M10-EC	0	-158,315	-672,369	-888,574
M20-EC	0	-133,285	-597,151	-882,360

	0 days	7 days	14 days	28 days
M0-CC	0	-28,198	-554,555	-703,377
M10-CC	0	-1,545	-550,971	-680,905
M20-CC	0	103,596	-402,572	-543,629

Figure 11 - Dimensional variation of M0, M10 and M20 under EC and CC at the ages of 7, 14 and 28 days

3.6 Dry bulk density, accessible porosity for water and carbonation depth

Dry bulk density and accessible porosity for water of M0, M10 and M20 under EC and CC at the ages of 28 days is shown in Figure . In both curing environments, replacing FA by MgO increased the mean dry bulk density values. This is due to the higher skeletal density of MgO (3400 kg/m^3) with respect to that FA (2431 kg/m^3). Curing in CO_2 further increased the dry bulk density due to the densification of the microstructure from the reaction of $Mg(OH)_2$ with CO_2 and the resulting precipitation of magnesium carbonates.

Interesting findings were observed for the accessible porosity to water; increasing MgO content led to lower values of porosity in samples cured in both environments, despite the contradictory worse mechanical performance. Normally, lower porosity is correlated with improved mechanical properties, but the opposite is seen here. It is likely that the use of MgO led to the formation of hydration products capable of filling voids and capillaries thereby reducing accessibility to water. This was more noticeable for MgO-containing specimens cured in the CO_2 chamber. The hydration products of MgO and resulting carbonated ones (i.e. brucite and nesquehonite) are platelet- and needle-shaped compounds, respectively, with little to no cohesion with adjacent phases, in comparison with the extensive polymerization products of AAM (i.e. N-A-S-H). Therefore, despite the void filling ability of MgO's products, which led to reduced porosity accessible to water, the lower connection of its products results in poorer mechanical performance.

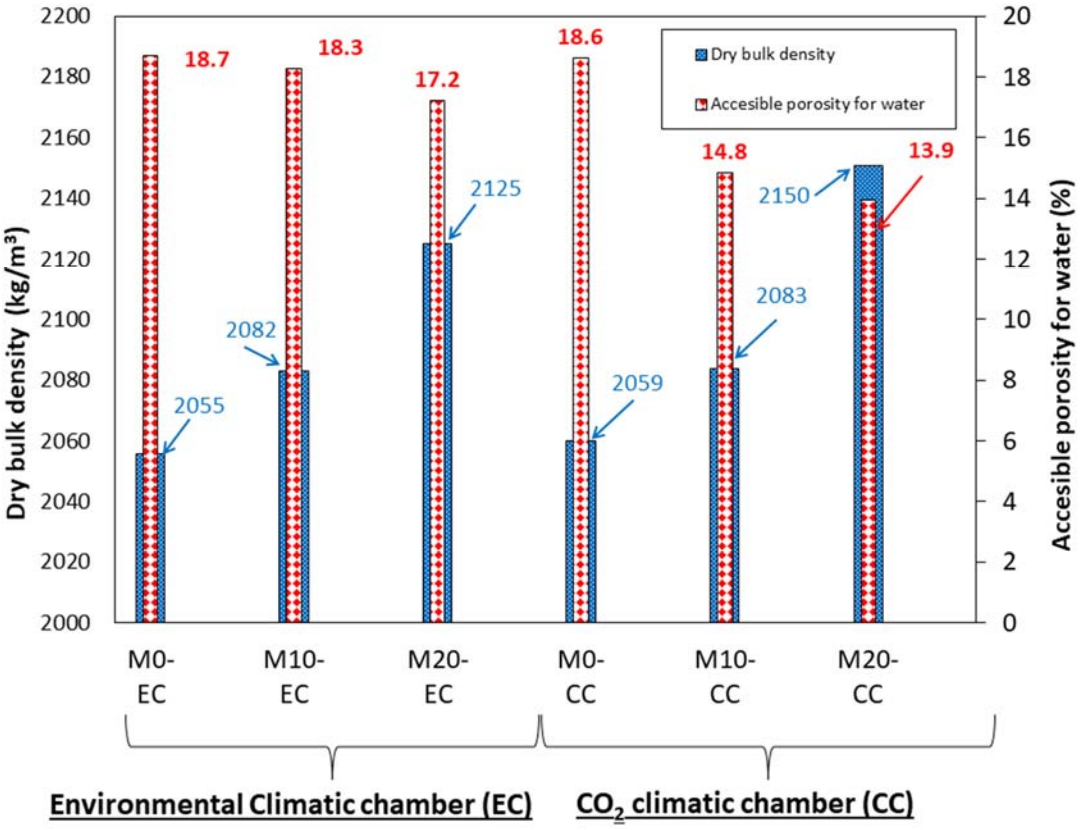

Figure 12 - Dry bulk density and accessible porosity for water of M0, M10 and M20 under EC and CC at the ages of 28 days

The carbonation depth of M0, M10 and M20 under EC and CC at the ages of 7, 14 and 28 days is shown in Figure . For specimens cured in the EC and exposed only to atmospheric CO_2, as expected, no carbonation was observed. Specimens cured in the CO_2 chamber presented notable depths of carbonation even after 7 days of curing. Nevertheless, it was significantly lower in specimens with increasing MgO content. $Mg(OH)_2$ increases the pH of the mixes and places additional material to become carbonated. This slows down the diffusion and thus carbonation depth (greater resistence to carbonation). Several authors also obtained an inverse relationship between natural carbonation depth and MgO content [49,74]. Other reason could be related to the formation of hydrotalcite [42]. Suescum-Morales et al. [55] have already confirmed the decrease in carbonation depth when the hydrotalcite is added to CBM. Note that under CC, the reference sample at the age of 28 days (M0-CC-28 days) did not have a high depth of carbonation (full carbonation would be at 20 mm). This highlights the higher resistance to carbonation of alkali-activated fly ash mortars compared to CBM [8].

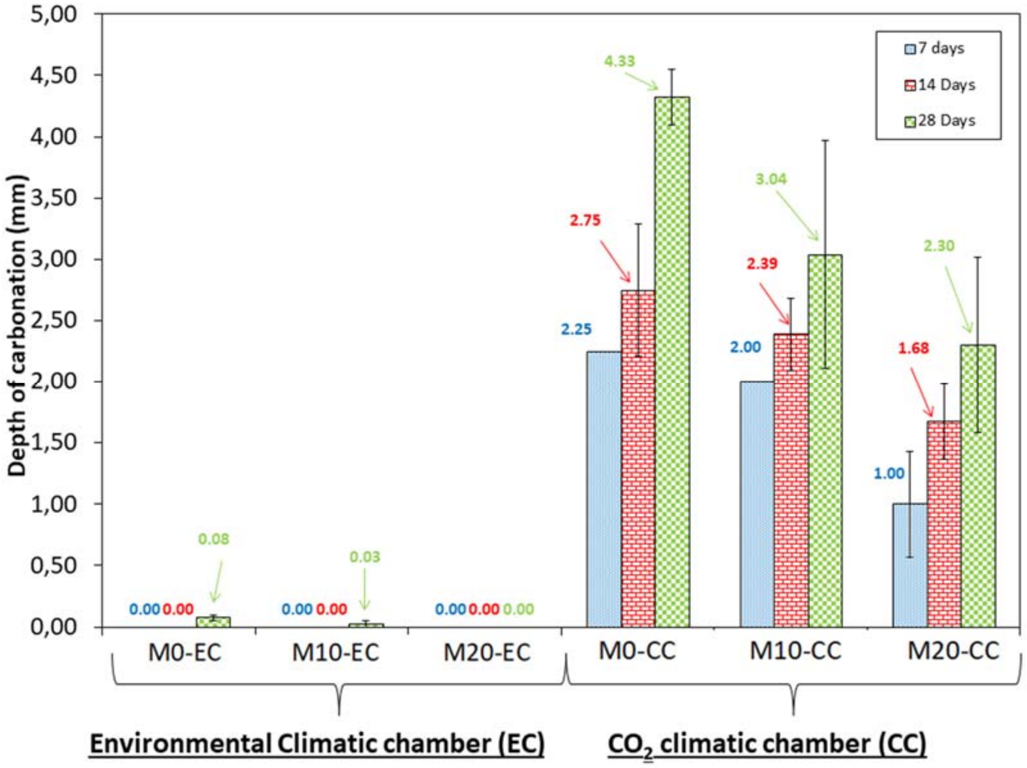

Figure 13 - Carbonation depth of M1, M2 and M3 under EC and CO_2-C at the ages of 7, 14 and 28 days

3.7 X-ray diffraction analysis

XRD patterns of M0, M10 and M20 cured in the EC and CC at the ages of 7 days are presented in Figure . The main phases of the reference sample cured in the EC (M1-EC-7 days) were: quartz (SiO_2) (05-0490) [83], mainly from CS and FS. Albite ($NaAlSi_3O_8$ - 89-6426) [83] and orthoclase ($KAlSi_3O_8$ - 75-1592) [83], from FS, were also found. Mullite (3 $Al_2O_3 \cdot 2SiO_2$ - 02-0431) [83] and calcite (05-0586) [83] also were partially observed in the patterns, coming from FA. The main reaction product was foshagite $Ca_4Si_3O_9 \cdot (OH)_2$ (74-0360) [83], most commonly known in the literature as calcium silicate hydrate gel (C-S-H). The chemical reaction process in AAM can be summarized in four steps [29]: (i) ion dissolution and release stage, i.e., dissolution of FA with the activator. The sodium (Na^+) and hydroxide ions (OH^-) in the activator quickly enter the system and attack the particles' surface, according to Eqs. 2 and 3. This step is deeply affected by the curing temperatures (high curing temperature catalyses OH^- activity); (ii) ion reconstitution stage, the main feature of this stage is the reconstruction and polycondensation of tetrahedral elements SiO_4 and AlO_4. Apart from the curing temperature, the role of water in the system is also important; (iii) hardening acceleration stage and (iv) hardening deceleration stage, the main feature of this stage is accelerated hardening. More macromolecules are condensed to form a gel, as C-S-H, which is in agreement with the findings in XRD. Several authors also found C-S-H as the main reaction products in AAM [42,75].

For the samples M10 and M20 cured in the EC at the age of 7 days, the same phases as those of M1 were observed, but brucite ($Mg(OH)_2$ - 02-1395) [83] was also found. Naturally, the intensity of brucite was higher for M3 than for M2. In addition, this result is in agreement with the results obtained in compressive and flexural strength, UPV, dynamic Young's modulus, dry bulk density, accessible porosity for water and shrinkage: formation of brucite, which is quite weak [79,93].

For specimens cured in the CC, at the age of 7 days, the XRD spectra of the reference sample are similar to the EC ones (M1-EC-7 days vs. M1-CO_2-C-7 days). N-A-S-H gel or partially carbonated C-(N)-A-S-H or $CaCO_3$ were not detected [101]. This may be due to the high degree of crystallinity of the quartz from the sand, which hides these amorphous/nano-crystalline elements (i.e. N-A-S-H and C-(N)-A-S-H gel). Apart from brucite, nesquehonite ($MgCO_3 \cdot 3H_2O$ - 20-0669) [83] was also found for M10 and M20 specimens. It showed a higher intensity with increasing MgO content. This phase forms when the brucite, under certain curing conditions, reacts with CO_2 to form a range of hydrated magnesium carbonates (HMCs) according to Eq. (5) [111], and likely to contribute towards strength development [78,79,112].

$$Mg(OH)_2 + CO_2 + 2\,H_2O \rightarrow MgCO_3 \cdot 3\,H_2O \qquad (5)$$

Hydrotalcite, which was expected to be observed in the spectrum, was not found possibly due to the high degree of crystallinity of the quartz. Another reason would be that the CaO content in the precursor (FA) should be about 30 %, and in this case it was around 7 % (see Table 2), as predicted by Ke and Duan [46]. Lee et al [78] did not find the hydrotalcite phase in XRD, attributing this fact to the formation of amorphous hydrotalcite instead of crystalline phases.

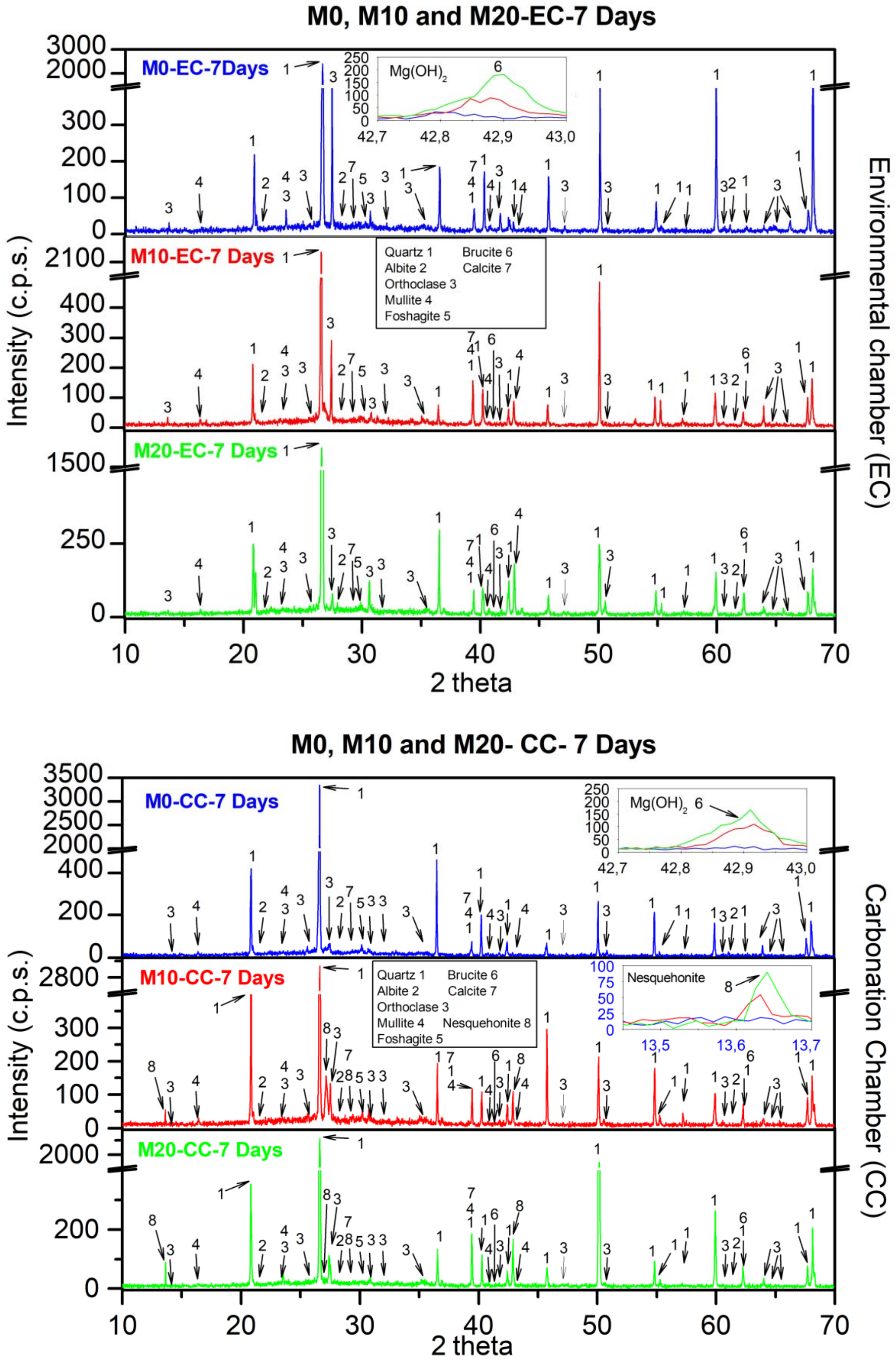

Figure 14 - XRD patterns of M0, M10 and M20 under EC and CC at the ages of 7 days

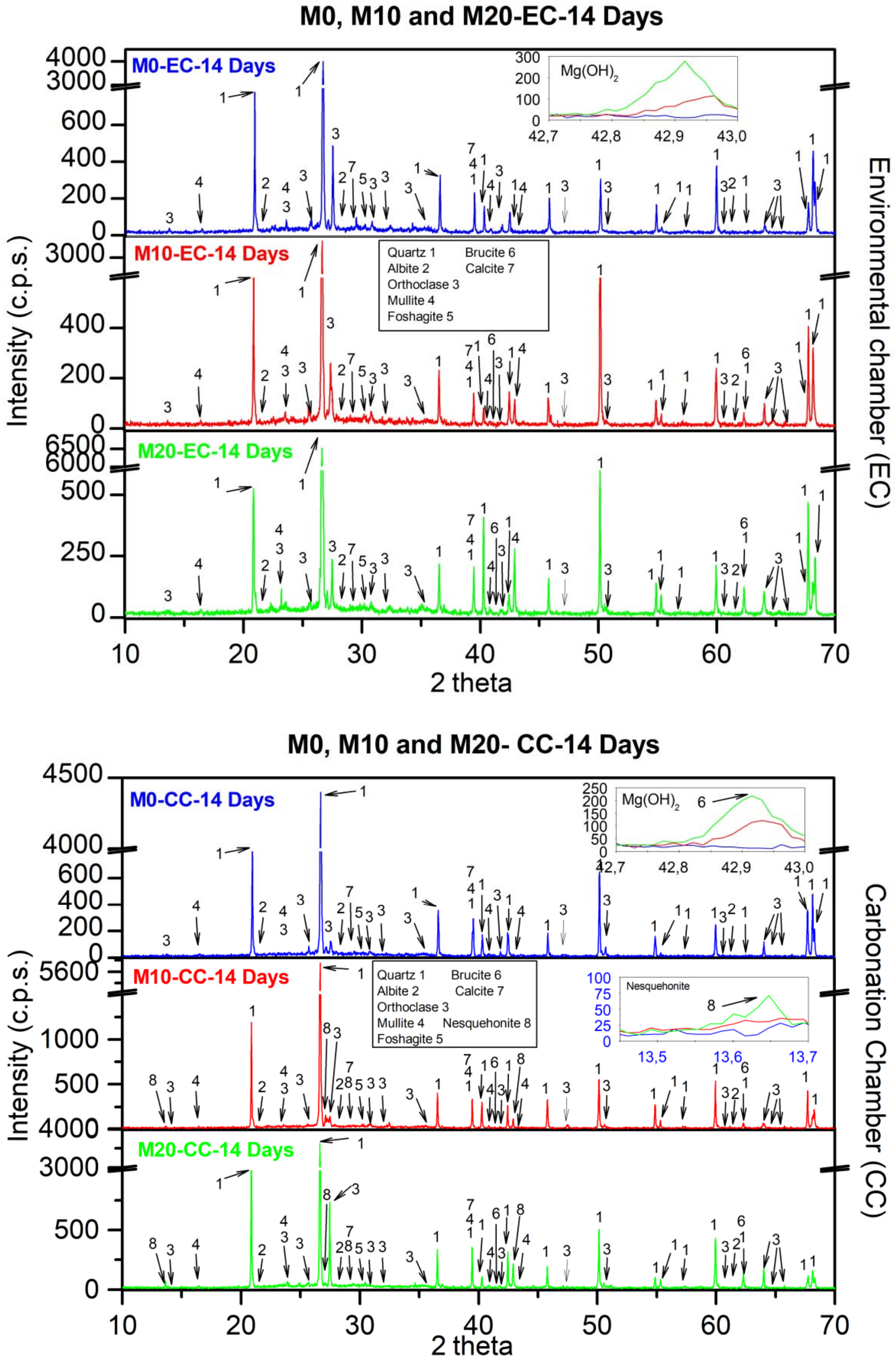
M0, M10 and M20-EC-14 Days

M0, M10 and M20- CC-14 Days

Figure 15 - XRD patterns of M0, M10 and M20 under EC and CC at the ages of 14 days

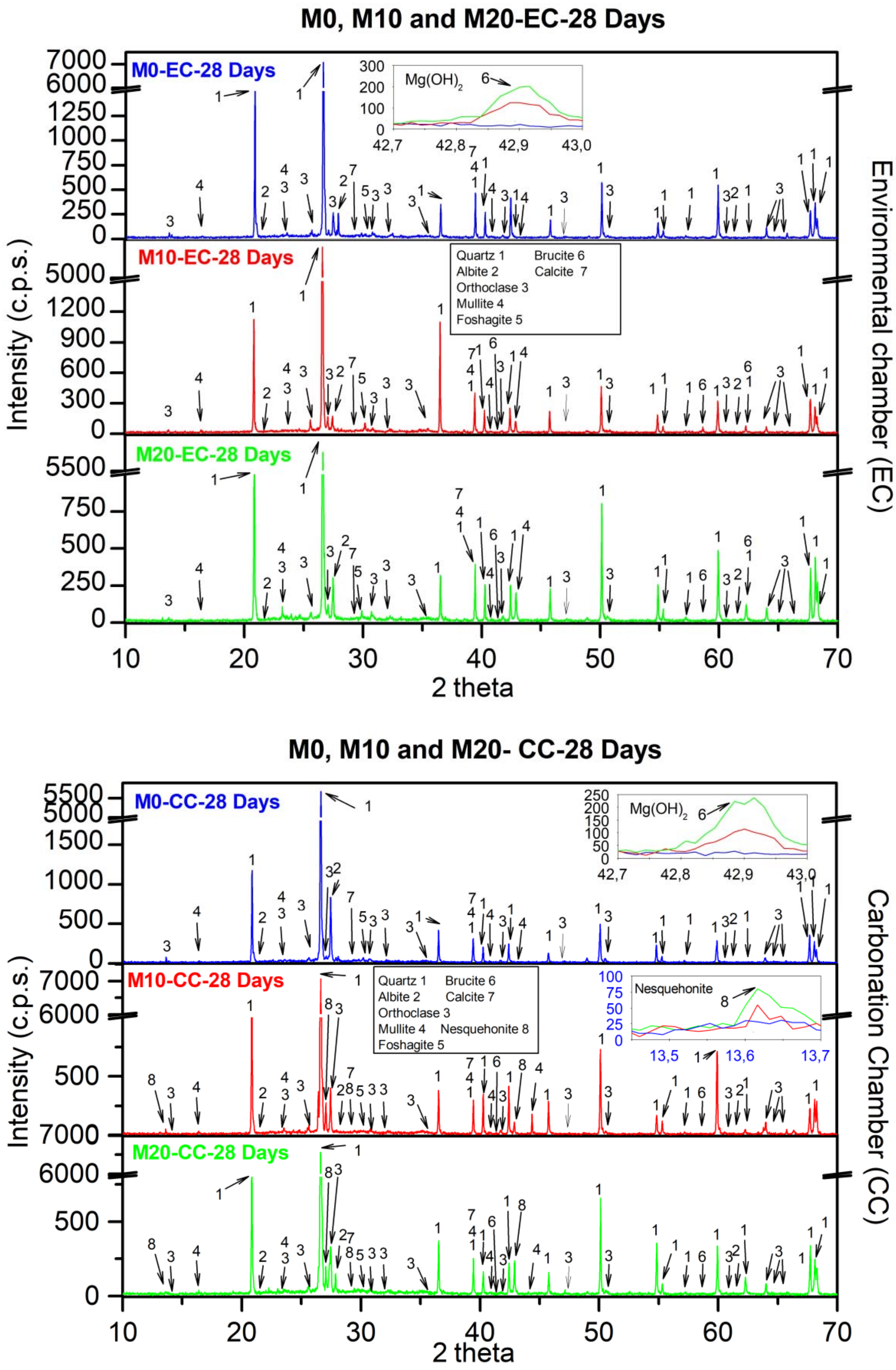

Figure 16 - XRD patterns of M0, M10 and M20 under EC and CC at the ages of 28 days

XRD patterns of M0, M10 and M20 under EC and CC at the ages of 14 and 28 days are presented in Figure 15 and Figure 16, respectively. The same phases as for age 7 days were found in both cases. Again under EC and CC, a higher amount of brucite was found as the amount of fly ash substitution for MgO. Under CC atmosphere, nesquehonite formation was also observed. Note that even at the age of 28 days, there was uncarbonated brucite (non-carbonated brucite). This is in agreement with the depth of carbonation shown in Fig. 13. The formation of weak and expansive brucite with the use of MgO justifies the worsening of the physical-mechanical properties under EC. The formation of nesquehonite with a dense formation and a needle-shaped morphology improves the physico-mechanical properties under CC.

3.8 Thermogravimetric analysis and differential thermal analysis

Figure 17 to Figure 19 show the TGA patterns (solid lines) and DTA (dotted lines) for the three mixes (M0, M10 and M20) under EC (A) and CC (B) at 7, 14 and 28 days of curing. Several stages were observed: (i) from room temperature to 105 ºC, the mass loss was due to the loss of hygroscopic water [79]; (ii) from 105 to 250 ºC, it was attributed mainly to the dehydration of C-S-H [43,44]; presented as the foshagite phase (C-S-H) in the XRD spectra of all samples. Some usually combine the two previous stages into a single one and attribute it to the dehydration of C-S-H and the evaporation of unbound water [32,49,73,76,110]. The dehydration of nesquehonite (HMCs) in carbonated M2 and M3 samples should also occur in this stage, according to Eq. (6) [79];

$$MgCO_3 \cdot 3H_2O \rightarrow MgCO_3 + 3\,H_2O \quad (6)$$

(iii) from 250 to 500 ºC, for 7-day specimens cured in both environments (Figure), only a peak in DTA was observed around 460 ºC due to the dihydroxylation of brucite, according to Eq. (7). However, in Figure 18 and Figure 19, a peak at approximately 390 ºC was also observed. This peak was due to the decomposition of a hydrotalcite-like phase formed specimens cured in both EC and CO_2-C. Lee et al. [78], who also detected this phase in TGA/DTA peaks, did not observe it in the XRD spectrum, attributing this fact to the formation of a non-crystalline hydrotalcite.

$$Mg(OH)_2 \rightarrow MgO + H_2O \qquad (7)$$

(iv) from 500 to 600 ºC, the decarbonation of magnesium carbonates to MgO begins according to Eq. (8) in M10 and M20 samples cured in the CO_2-C [79]. In this stage, an endothermic peak was detected around 570 ºC corresponding to the transformation in the crystal structure of the sand (FS and CS) of the phase from quartz α to β [96]. In this stage, the calcium carbonate decomposition also begins according to Eq. (1) [2]. (v) from 600 to 1000 ºC the decarbonation of magnesium carbonate to MgO and calcium carbonate decomposition continue [2,79].

$$MgCO_3 \rightarrow MgO + CO_2 \qquad (8)$$

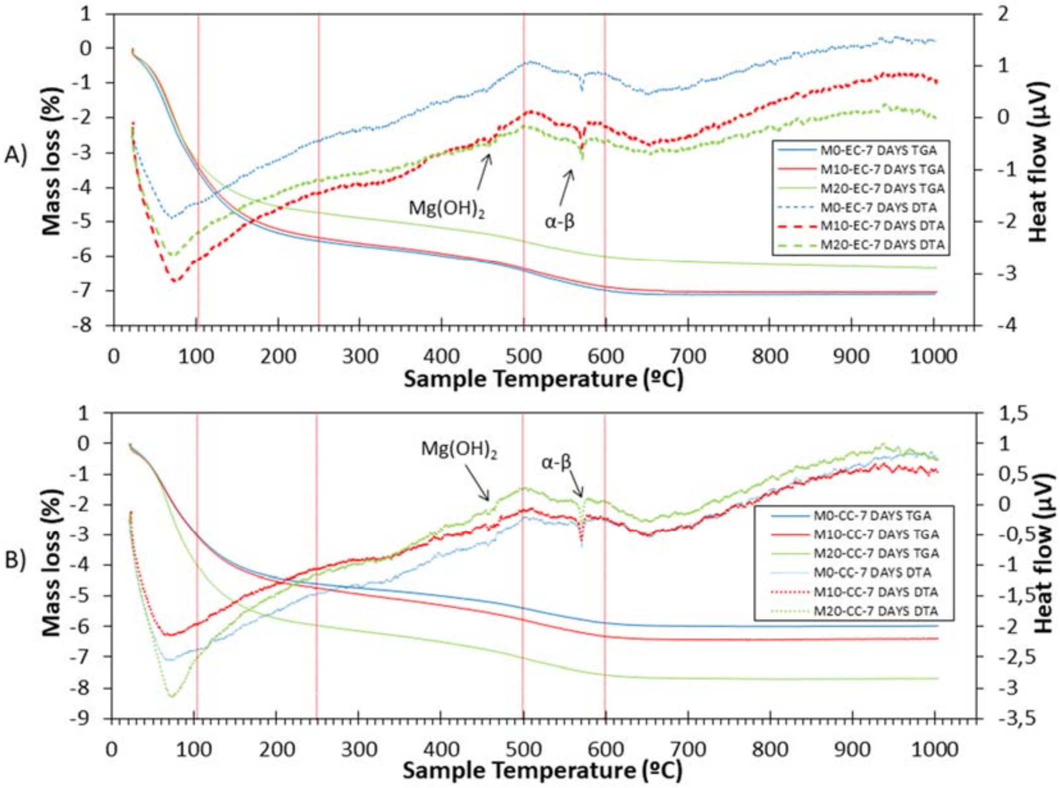

Figure 17 - TGA (solid lines) and DTA (dotted lines) of M0, M10 and M20 under EC and CC at the ages of 7 days

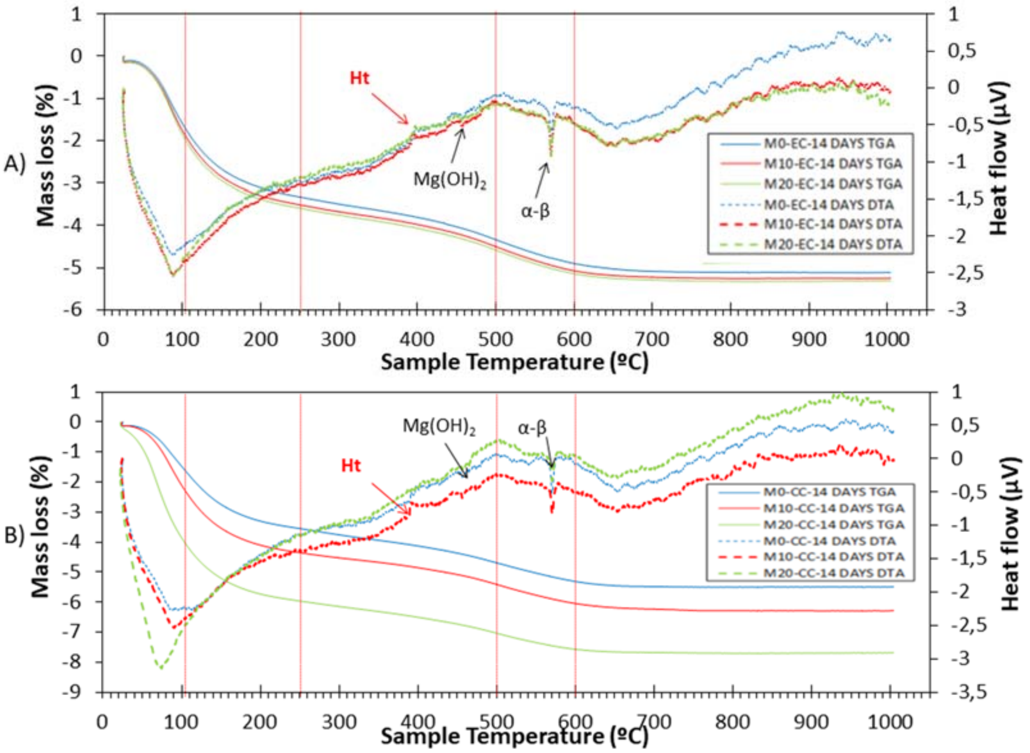

Figure 18 - TGA (solid lines) and DTA (dotted lines) of M0, M10 and M20 under EC and CC at the ages of 14 days

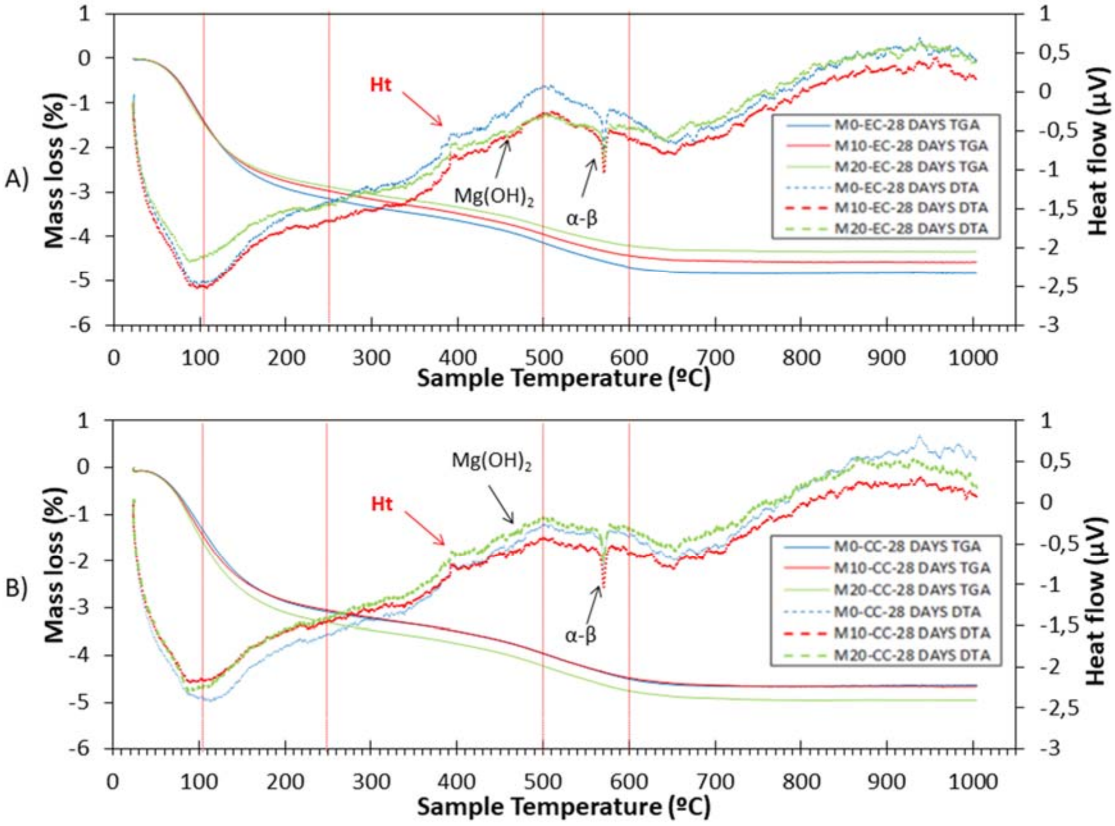

Figure 19 - TGA (solid lines) and DTA (dotted lines) of M0, M10 and M20 under EC and CC at the ages of 28 days

The CO_2 stored by the samples can be calculated via the TGA results. Table shows the total mass loss in TGA/DTA of all samples. The CO_2 captured by the samples has been calculated as the loss of mass between 250 and 1000 ºC. The range between 250-1000 ºC was chosen because: (i) the decomposition of hydrotalcite between 250-500 ºC was observed in some samples, which can capture CO_2 [1,55] (ii) between 500-1000 ºC the decomposition of nesquehonite occurred (Eq. 6). Since the decomposition of calcium carbonate also occurred between 500 and 1000 ºC, the CO_2 captured have been normalized with the reference sample (M0-CC-7 Days). In this way, two factors were taken into account in the CO_2 stored by the samples: (i) the substitution of FA by MgO and (ii) the increase of the CO_2 level in curing. A similar procedure has been used by Caslin and White [76].

Naturally, the amount of captured CO_2 increased with curing time and was higher in specimens cured in the CO_2-C. Also, higher amounts of MgO led to a greater sequestration of CO_2 (M3>M2). The increase in mass between due to CO_2 capture was of 6.91%, 9.39% and 12.26% at the age of 7, 14 and 28 days, respectively, when compared to mixes cured in the EC vs. CC (M3-EC vs. M3-CO_2-C). Replacing 20% FA with MgO led to the absorption of ~2 g CO_2/kg of the specimen after 28 days of CO_2-C curing when compared to the reference EC sample with the same curing age. These results indicate that the increased CO_2 capture of these materials relies on two fundamental factors: (i) replacement level of FA by MgO and; (ii) CO_2 content in the curing environment. Similar calculations have not been found in alkali activated fly ash mortars.

Table 3 - Total mass loss in thermogravimetric analysis (TGA/DTA) for the differents mixes and CO$_2$ uptake

Mixes	Δ mass (%)					Δ mass (250-1000 ºC)	Normalized CO$_2$ (wt.%)
	RT-105 ºC	105-250 ºC	250-500 ºC	500-600 ºC	600-1000 ºC		
M0-EC-7 Days	-3.609	-1.936	-0.877	-0.563	-0.103	1.543	1.000
M10-EC-7 Days	-3.476	-1.974	-0.902	-0.533	-0.141	1.576	1.021
M20-EC-7 Days	-3.326	-1.397	-0.836	-0.446	-0.326	1.608	1.042
M0-CC-7 Days	-3.037	-1.561	-0.800	-0.484	-0.269	1.553	1.006
M10-CC-7 Days	-3.084	-1.651	-1.049	-0.540	-0.064	1.652	1.070
M20-CC-7 Days	-4.058	-1.903	-1.071	-0.536	-0.113	1.720	1.114
M0-EC-14 Days	-1.750	-1.575	-0.851	-0.497	-0.215	1.563	1.013
M10-EC-14 Days	-1.919	-1.592	-0.902	-0.533	-0.174	1.610	1.043
M20-EC-14 Days	-2.020	-1.571	-0.940	-0.539	-0.165	1.645	1.066
M0-CC-14 Days	-1.639	-1.912	-0.900	-0.522	-0.177	1.599	1.036
M10-CC-14 Days	-2.314	-2.040	-0.904	-0.572	-0.235	1.709	1.107
M20-CC-14 Days	-4.058	-1.903	-1.127	-0.558	-0.114	1.800	1.166
M0-EC-28 Days	-1.422	-1.730	-0.941	-0.539	-0.121	1.601	1.037
M10-EC-28 Days	-1.431	-1.542	-1.007	-0.493	-0.141	1.640	1.063
M20-EC-28 Days	-1.489	-1.391	-1.067	-0.502	-0.132	1.701	1.102
M0-CC-28 Days	-1.344	-1.739	-0.935	-0.565	-0.131	1.631	1.057
M10-CC-28 Days	-1.463	-1.584	-1.047	-0.575	-0.180	1.801	1.167
M20-CC-28 Days	-1.600	-1.710	-1.107	-0.610	-0.192	1.909	1.237

3.9 Scanning electron microscopy

Figure shows the SEM micrographs and general EDS mapping of the reference sample cured in the EC after 28 days. Several zones of interest are immediately observable: micro-cracks; voids; rounded growths; and unreacted FA particles. The micro-cracks may be attributed to the evaporation of water during the thermal curing stage at a temperature of 70 ºC [113] Additionally, the ongoing reaction process, leading to the formation of dense products from initially more voluminous ones, may also lead to the generation of localized stresses that ultimately cause cracking. In addition to their spherical shape, unreacted FA particles were detected in SEM-EDS analysis. These particles did not show the presence of Ca, which in agreement with the low amount of Ca found in XRF (Table 2), XRD (Figure 2) and TGA/DTA (Figure 4). The presence of the spherical voids is likely due to the removal of unreacted FA particles during the polishing process. The rounded growths consist of N-A-S-H gel and partially dissolved FA particles enveloped by it [114]. This phase had not been found in XRD because it is an amorphous phase, and the high intensity of other crystalline phases may have masked it. The main elements from FA were Si and Al, and Ca in minor proportions. This result is in accordance with the FA particles' EDS mapping (Figure a), chemical composition (Table 2) and XRD results (Figure). Additional minor elements were detected: Na, C, K and Fe as also observed in the XRF of the precursor (Table 2).

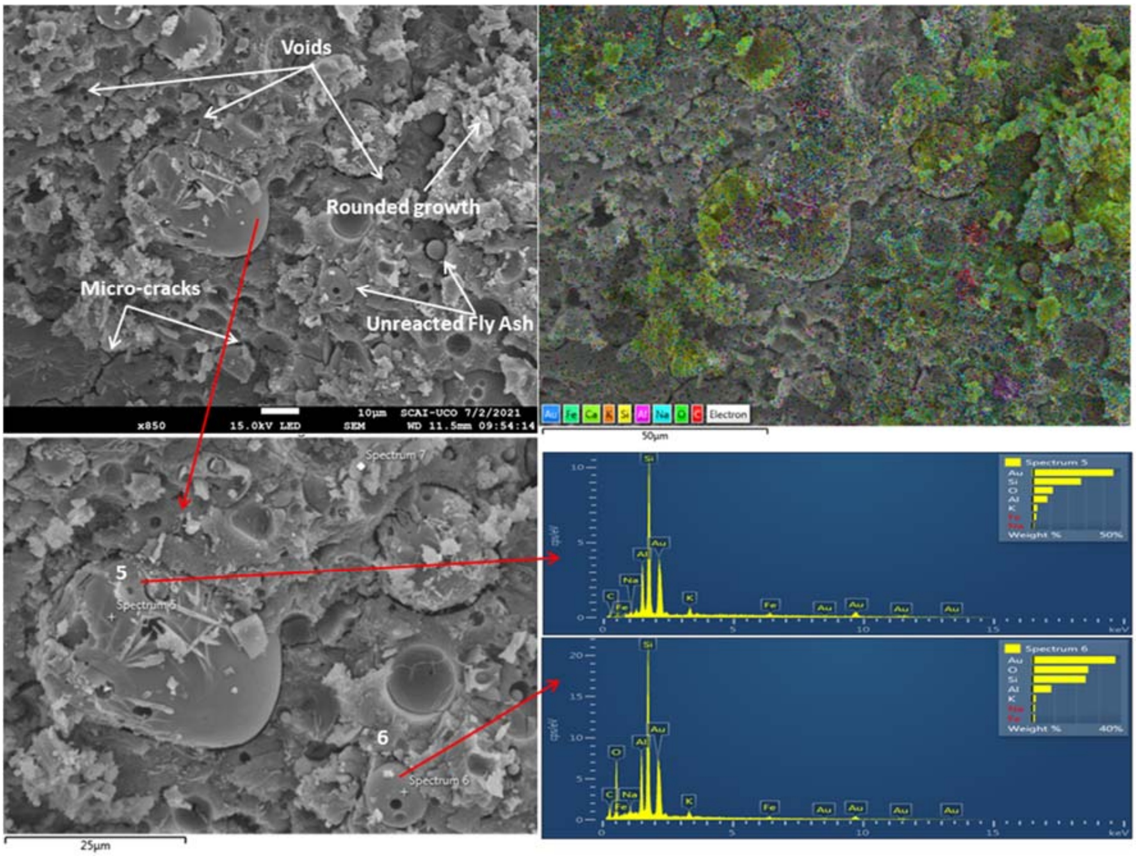

Figure 20 - SEM images and EDS of M0-EC-28 days. Mapping with the identification of the elements Si, Al, Ca, Na, C, K and Fe.

Figure shows the SEM micrographs and general EDS mapping of the reference sample cured in the CO_2-C for 28 days. It corresponds to one edge of the specimen in order to observe the effect of CO_2 on the samples' surface. All samples subjected to CO_2 presented significant efflorescence. Excess Na^+ becomes more mobile within the pore structure of the alkali-activated FA mortars, and, when in contact with CO_2, it forms white crystals corresponding to sodium carbonates (efflorescence) [8,24,100]. Micro-cracks, rounded growths and unreacted FA particles were also observed, although with a lower number that under EC [69]. Practically no gaps were observed. This result could be related to the formation of insoluble calcium carbonate and densifying of the microstructure, which can also occur in fly ash systems activated by calcium-rich alkalis [8,100–102,115]. This densification of the microstructure is in accordance with the observed decrease in shrinkage (Fig. 11) and the slight improvement in mechanical properties (Figs. 7-10).

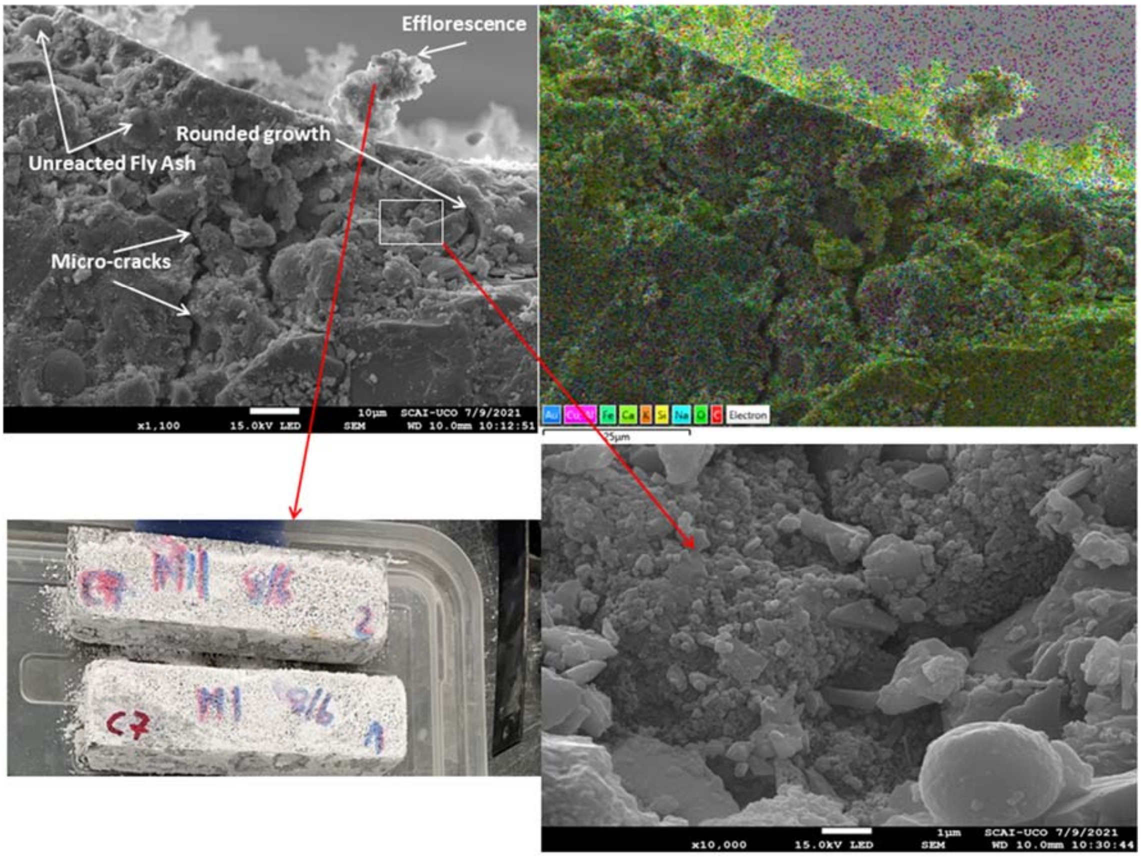

Figure 21 - SEM images of M0-CC-28 days. Mapping with the identification of the elements Si, Al, Ca, Na, C, K and Fe.

Figure shows the SEM micrographs and EDS analysis M20-EC after 28 days of curing. Two main zones were observed: aggregate and binder. The interfacial transition zone (ITZ) was very sound; no gaps were observed, indicating perfect cohesion. Apart from Mg, the EDS mapping revealed essentially the same elements as those in the reference sample. This is also in agreement with the decrease on the mechanical properties (Figs. 7 and 8), UPV (Fig. 9), and Dynamic Young Modulus (Fig. 10) observed with the use of MgO and with the presence of brucite ($Mg(OH)_2$) found in XRD (Figs. 15-17) which is quite weak [79,93]. Inside the binder, again the following were observed just some micro-cracks, rounded growths and unreacted fly ash were observed. There was a perfect fusion between the Mg and the other elements into a single uniform binding material. The lower amount of micro-cracks observed may be related to the expansivity of the brucite [42,108,109] and with the lowest shrinkage observed with the use of MgO (Fig. 11).

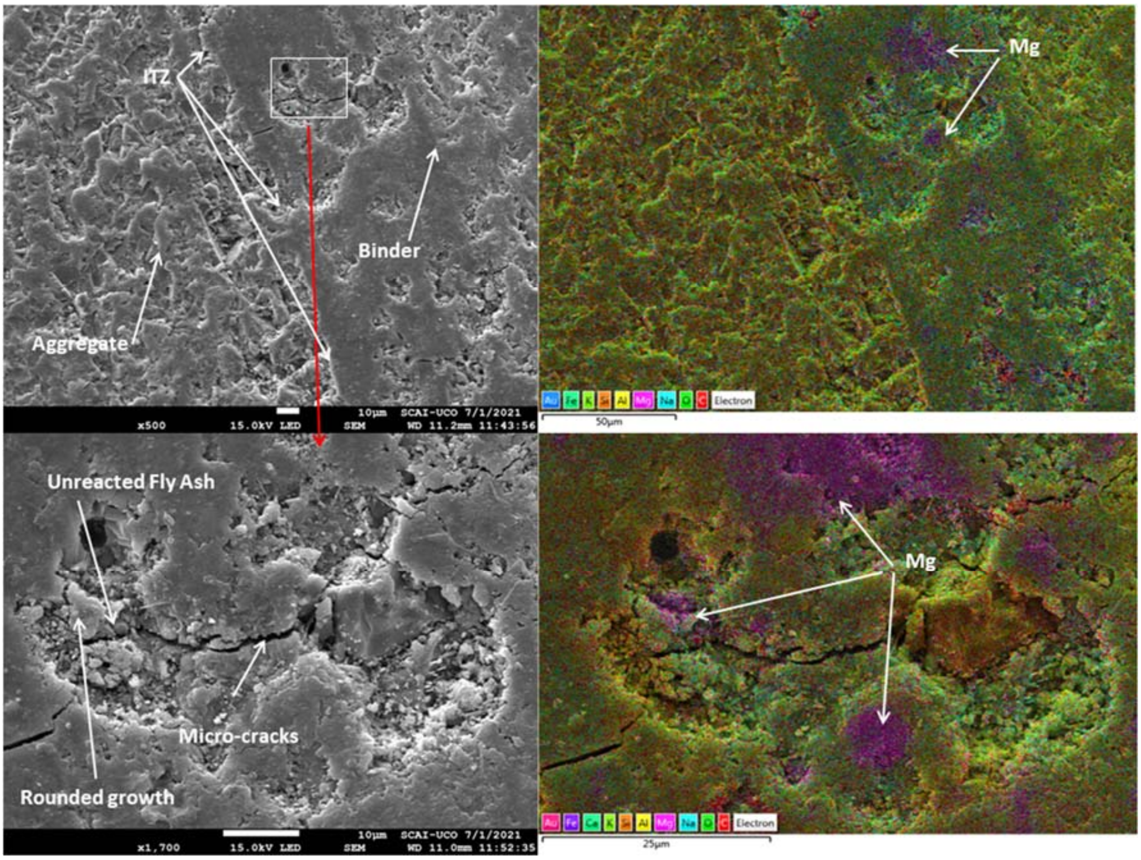

Figure 22 - SEM images of M20-EC-28 days with the identification of micro-cracks, unreacted fly ash and rounded growth. Mapping with the identification of the elements Si, Al, Ca, Na, C, K , Fe and MgO.

Figure shows the SEM micrographs and elemental mapping of a M3 sample cured in the CO_2-C for 28 days. It corresponds to the edge of the sample to understand the effect of CO_2. At a low magnification, generally, micro-cracks and unreacted FA particles were difficult to observe, as most of them had reacted [69]. At a higher magnification, in the Mg-rich area, the formation of nesquehonite ($MgCO_3 \cdot 3H_2O$) was observed. Two morphologies were detected for this compound: needle-like morphology (typical elongated habit) [116] and a dense formation more round that could be a mixture of brucite and nesquehonite [79,117]. This is in agreement with the phases found in XRD.

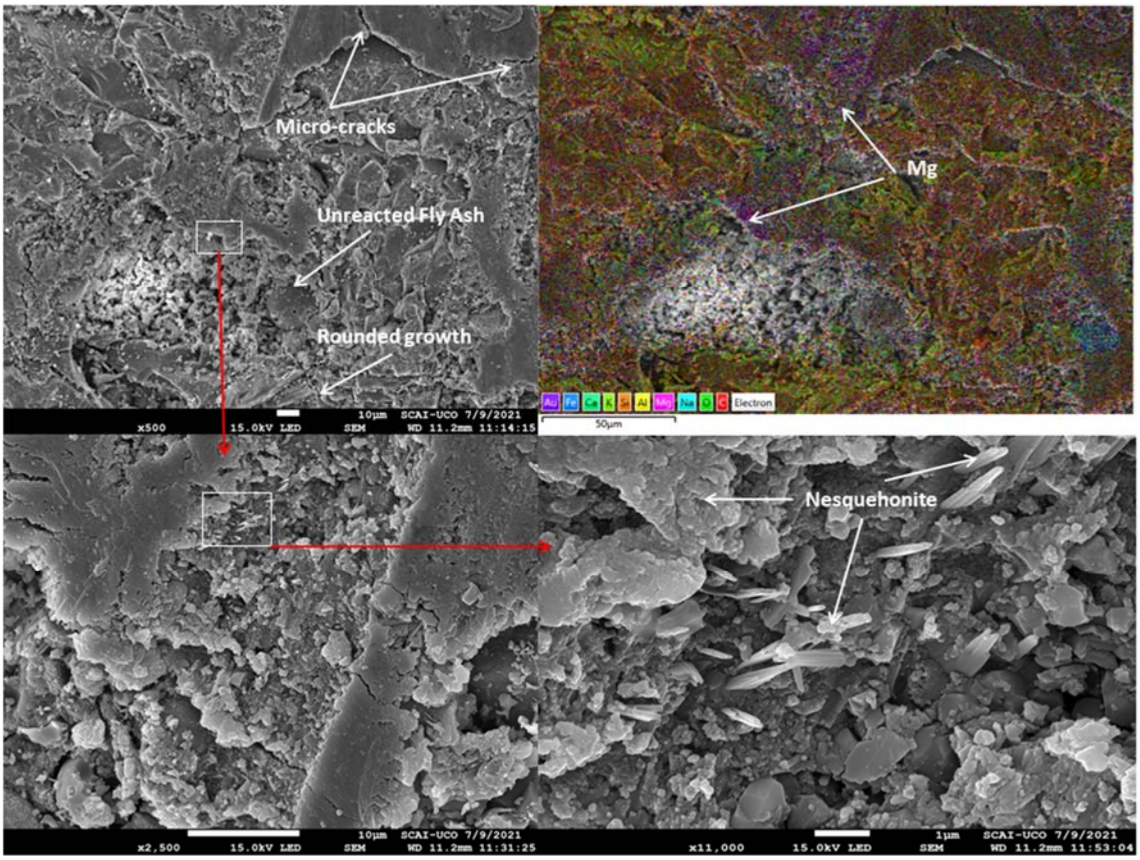

Figure 23 - SEM micrographs of M20-CC-28 days. Mapping with the identification of the elements Si, Al, Ca, Na, C, K , Fe and MgO.

4. Conclusions

This study shows the effect of reactive magnesium oxide as partial replacement of fly ash in alkali-activated mortars under two different curing environments: normal climatic chamber or accelerated carbonation chamber. First, a complete characterization of all raw materials had been carried out. The mortars' physical-mechanical properties (compressive and flexural strength, ultrasonic pulse velocity, dynamic Young's modulus, dry bulk density and accessible porosity for water) were evaluated. The relationships between these properties were further explained through other test methods such as carbonation depth, shrinkage, XRD, SEM and TGA/DTA. The following conclusions were drawn:

- Consistence decreased and the bulk density of fresh mortar increased with increasing MgO content; FA particles convey a "lubricating" effect for fresh mortars and are less dense than MgO particles.

- Replacing FA with MgO resulted in an overall decline in performance (i.e. compressive and flexural strengths, ultrasonic pulse velocity, dynamic Young's modulus) for specimens cured in both environments. This was mainly due to the formation of relatively weak and expansive brucite (detected by XRD) and formation of hydrotalcite (detected by TGA/DTA).
- Despite the decline in the performance, the accessible porosity for water and depth of carbonation decreased. The hydration products of MgO presented a void-filling ability capable of reducing water movement and slowing down CO_2 diffusion. Additionally, the presence of $Mg(OH)_2$ increased the matrix's pH level ("lower carbonation depth" via the phenolphthalein indicator) and the number of compounds that could be consumed by CO_2 thereby reducing its progression.
- CO_2 curing resulted in generally enhanced performance. For the reference sample, without MgO, this was due mainly to formation of insoluble calcium carbonate (densification of the microstructure in SEM) and for samples with MgO was observed the formation of hydrated magnesium carbonates (HMCs), mainly nesquehonite ($MgCO_3 \cdot 3H_2O$)). For further researches the analysis has to be carried out in terms of the presence of Si—O bridges due to the desodification of N-A-S-H phases (FTIR).
- The hydrotalcite phase was not found in XRD (high degree of crystallinity of the quartz). Nevertheless, the hydrotalcite was detected with TGA/DTA.
- The substitution of 20% FA with MgO under CO_2 curing resulted in an improvement of CO_2 absorption capacity compared to the reference sample cured in a normal climatic chamber at the same age of curing. The amount of CO_2 captured was 2 g CO_2/kg specimen after 28 days of curing.
- SEM revealed the densification of the microstructure of the reference sample with CO_2 curing. SEM showed that the effect of replacing FA with MgO and the CO_2 curing resulted in a dense formation and needle-like morphology (nesquehonite).

The partial use of reactive MgO in alkali-activated FA mortars cured in CO_2 is a promising promote the new circular economy paradigm in the construction sector, act as CO_2 sinks and avoid the consumption of ordinary Portland cement.

Declaration of competing interest

The authors declare that they have no known competing financial interest or personal relationships that could have appeared to influence the work reported in this paper

Acknowledgments

The authors would like to acknowledge the financial support from the Ministry of Science and Innovation (Ministerio de Ciencia e Innovación, Spanish government) through the PRECAST research project (Ref. PID2019-111029RB-I00) and FCT- Foundation for Science and Technology, through the research project PTDC/ECI- CON/29196/2017 (RInoPolyCrete), PTDC/ECI-CON/31138/2017 (DecarbonCrete) and EXPL/ECIEGC/0288/2021 (ECO2Alkrete). This work is also part of the research activity carried out at Civil Engineering Research and Innovation for Sustainability (CERIS) in the framework of project UIDB/04625/2020 funded by FCT. The authors wish to thank the IE57164 project for the implementation and improvement of scientific and technological infrastructures and equipment supported by the Andalusian regional government (FEDER 2011). D. Suescum-Morales also acknowledges funding from MECD-Spain (http://www.mecd.-gob.es/educacion-mecd/) FPU 17/04329 and to the University of Cordoba for the funding offered for a stay at IST Lisbon (BOUCO 2020/00527).

References

[1] D. Suescum-Morales, D. Cantador-Fernández, J.M. Fernández, J.R. Jiménez, Mitigation of CO2 emissions by hydrotalcites of Mg3Al-CO3 at 0 ◦C and high pressure, Appl. Clay Sci. (2020). doi:doi.org/10.1016/j.clay.2020.105950.

[2] D. Suescum-Morales, K. Kalinowska-wichrowska, J.M. Fernández, J.R. Jiménez, Accelerated carbonation of fresh cement-based products containing recycled

masonry aggregates for CO2 sequestration, J. CO2 Util. 46 (2021). doi:10.1016/j.jcou.2021.101461.

[3] D. Suescum-Morales, D. Cantador-Fernández, J.M. Fernández, J.R. Jiménez, The combined effect of CO2 and calcined hydrotalcite on one-coat limestone mortar properties, Constr. Build. Mater. 280 (2020) 122532. doi:10.1016/j.conbuildmat.2021.122532.

[4] E. Benhelal, G. Zahedi, E. Shamsaei, A. Bahadori, Global strategies and potentials to curb CO2 emissions in cement industry, J. Clean. Prod. 51 (2013) 142–161. doi:10.1016/j.jclepro.2012.10.049.

[5] R. Carvalho, R. V. Silva, J. de Brito, M.F.C. Pereira, Alkali activation of bottom ash from municipal solid waste incineration: Optimization of NaOH- and Na 2SiO3-based activators, J. Clean. Prod. 291 (2021) 125930. doi:10.1016/j.jclepro.2021.125930.

[6] T. Luukkonen, Z. Abdollahnejad, J. Yliniemi, P. Kinnunen, M. Illikainen, One-part alkali-activated materials: A review, Cem. Concr. Res. 103 (2018) 21–34. doi:10.1016/j.cemconres.2017.10.001.

[7] J.S. Damtoft, J. Lukasik, D. Herfort, D. Sorrentino, E.M. Gartner, Sustainable development and climate change initiatives, Cem. Concr. Res. 38 (2008) 115–127. doi:10.1016/j.cemconres.2007.09.008.

[8] M. Amran, S. Debbarma, T. Ozbakkaloglu, Fly ash-based eco-friendly geopolymer concrete: A critical review of the long-term durability properties, Constr. Build. Mater. 270 (2021) 121857. doi:10.1016/j.conbuildmat.2020.121857.

[9] Z. Chen, J.S. Li, B.J. Zhan, U. Sharma, C.S. Poon, Compressive strength and microstructural properties of dry-mixed geopolymer pastes synthesized from GGBS and sewage sludge ash, Constr. Build. Mater. 182 (2018) 597–607. doi:10.1016/j.conbuildmat.2018.06.159.

[10] C.K. Ma, A.Z. Awang, W. Omar, Structural and material performance of geopolymer concrete: A review, Constr. Build. Mater. 186 (2018) 90–102. doi:10.1016/j.conbuildmat.2018.07.111.

[11] N. Li, C. Shi, Z. Zhang, H. Wang, Y. Liu, A review on mixture design methods for geopolymer concrete, Compos. Part B Eng. 178 (2019) 107490. doi:10.1016/j.compositesb.2019.107490.

[12] M. Wasim, T.D. Ngo, D. Law, A state-of-the-art review on the durability of geopolymer concrete for sustainable structures and infrastructure, Constr. Build. Mater. 291 (2021) 123381. doi:10.1016/j.conbuildmat.2021.123381.

[13] B.S. Thomas, J. Yang, K.H. Mo, J.A. Abdalla, R.A. Hawileh, E. Ariyachandra, Biomass ashes from agricultural wastes as supplementary cementitious materials or aggregate replacement in cement/geopolymer concrete: A comprehensive review, J. Build. Eng. 40 (2021) 102332. doi:10.1016/j.jobe.2021.102332.

[14] P. Nath, P.K. Sarker, Fly ash based geopolymer concrete: A review, ISEC 2013 - 7th Int. Struct. Eng. Constr. Conf. New Dev. Struct. Eng. Constr. (2013) 1091–1096. doi:10.3850/978-981-07-5354-2-M-54-431.

[15] S. Parathi, P. Nagarajan, S.A. Pallikkara, Ecofriendly geopolymer concrete: a comprehensive review, Clean Technol. Environ. Policy. 23 (2021) 1701–1713. doi:10.1007/s10098-021-02085-0.

[16] Y. Alrefaei, Y.S. Wang, J.G. Dai, Effect of mixing method on the performance of alkali-activated fly ash/slag pastes along with polycarboxylate admixture, Cem. Concr. Compos. 117 (2021) 103917. doi:10.1016/j.cemconcomp.2020.103917.

[17] J. Davidovits, Society of Plastic Engineering, Brookf. Cent. (1979).

[18] J.L. Provis, Alkali-activated materials, Cem. Concr. Res. 114 (2018) 40–48. doi:10.1016/j.cemconres.2017.02.009.

[19] R. Siddique, Utilization of silica fume in concrete: Review of hardened properties, Resour. Conserv. Recycl. 55 (2011) 923–932. doi:10.1016/j.resconrec.2011.06.012.

[20] H. Zhao, W. Sun, X. Wu, B. Gao, The properties of the self-compacting concrete with fly ash and ground granulated blast furnace slag mineral admixtures, J. Clean. Prod. 95 (2015) 66–74. doi:10.1016/j.jclepro.2015.02.050.

[21] M. Nodehi, V.M. Taghvaee, Alkali-Activated Materials and Geopolymer: a Review of Common Precursors and Activators Addressing Circular Economy, Circ. Econ. Sustain. (2021). doi:10.1007/s43615-021-00029-w.

[22] R. Xiao, X. Jiang, M. Zhang, P. Polaczyk, B. Huang, Analytical investigation of phase assemblages of alkali-activated materials in CaO-SiO2-Al2O3 systems: The management of reaction products and designing of precursors, Mater. Des. 194 (2020) 108975. doi:10.1016/j.matdes.2020.108975.

[23] R.A. Robayo-Salazar, R. Mejía de Gutiérrez, Natural volcanic pozzolans as an available raw material for alkali-activated materials in the foreseeable future: A review, Constr. Build. Mater. 189 (2018) 109–118.

doi:10.1016/j.conbuildmat.2018.08.174.

[24] M.R. Ahmad, B. Chen, S.F.A. Shah, Influence of different admixtures on the mechanical and durability properties of one-part alkali-activated mortars, Constr. Build. Mater. 265 (2020) 120320. doi:10.1016/j.conbuildmat.2020.120320.

[25] J. Davidovits, Geopolymers: man-made rock geosynthesis and the resulting development of very early high strength cement, J.Mater.Educ. 16 (2) (1994) 91–139.

[26] J. Yuan, L. Li, P. He, Z. Chen, C. Lao, D. Jia, Y. Zhou, Effects of kinds of alkali-activated ions on geopolymerization process of geopolymer cement pastes, Constr. Build. Mater. 293 (2021) 123536. doi:10.1016/j.conbuildmat.2021.123536.

[27] G.S. Ryu, Y.B. Lee, K.T. Koh, Y.S. Chung, The mechanical properties of fly ash-based geopolymer concrete with alkaline activators, Constr. Build. Mater. 47 (2013) 409–418. doi:10.1016/j.conbuildmat.2013.05.069.

[28] K.A. Komnitsas, Potential of geopolymer technology towards green buildings and sustainable cities, Procedia Eng. 21 (2011) 1023–1032. doi:10.1016/j.proeng.2011.11.2108.

[29] X. Wei, D. Li, F. Ming, C. Yang, L. Chen, Y. Liu, Influence of low-temperature curing on the mechanical strength, hydration process, and microstructure of alkali-activated fly ash and ground granulated blast furnace slag mortar, Constr. Build. Mater. 269 (2021) 121811. doi:10.1016/j.conbuildmat.2020.121811.

[30] E. Pawluczuk, K. Kalinowska-Wichrowska, J.R. Jiménez, J.M. Fernández, D.

Suescum-Morales, Geopolymer concrete with treated recycled aggregates: Macro and microstructural behavior, J. Build. Eng. 44 (2021) 103317. doi:10.1016/j.jobe.2021.103317.

[31] G. Li, H. Tan, J. Zhang, X. Deng, X. Liu, Z. Luo, Ground granulated blast-furnace slag/fly ash blends activated by sodium carbonate at ambient temperature, Constr. Build. Mater. 291 (2021) 123378. doi:10.1016/j.conbuildmat.2021.123378.

[32] R. Sun, C. Fang, H. Zhang, Y. Ling, J. Feng, H. Qi, Z. Ge, Chemo-mechanical properties of alkali-activated slag/fly ash paste incorporating white mud, Constr. Build. Mater. 291 (2021) 123312. doi:10.1016/j.conbuildmat.2021.123312.

[33] Q. Fu, W. Xu, X. Zhao, M. Bu, Q. Yuan, D. Niu, The microstructure and durability of fly ash-based geopolymer concrete : A review, Ceram. Int. (2021). doi:10.1016/j.ceramint.2021.07.190.

[34] P. Zhang, Z. Gao, J. Wang, J. Guo, S. Hu, Y. Ling, Properties of fresh and hardened fly ash/slag based geopolymer concrete: A review, J. Clean. Prod. 270 (2020) 122389. doi:10.1016/j.jclepro.2020.122389.

[35] S. V Patil, V.B. Karikatti, M. Chitawadagi, Granulated Blast-Furnace Slag (GGBS) based Geopolymer Concrete - Review, 5 (2018).

[36] M. Criado, J.L. Provis, Alkali activated slag mortars provide high resistance to chloride-induced corrosion of steel, Front. Mater. 5 (2018) 1–15. doi:10.3389/fmats.2018.00034.

[37] T. Bakharev, J.G. Sanjayan, Y.B. Cheng, Resistance of alkali-activated slag

concrete to acid attack, Cem. Concr. Res. 33 (2003) 1607–1611. doi:10.1016/S0008-8846(03)00125-X.

[38] Xinyuan Ke, S. A. Bernal, Tsutomu Sato, J. L. Provis, Alkali aluminosilicate geopolymers as binders to encapsulate strontium-selective titanate ion-exchangers, Dalt. Trans. 48 (2019) 12116–12126. doi:10.1039/C9DT02108F.

[39] R. Wang, N. Mirza, D.G. Vasbieva, Q. Abbas, D. Xiong, The nexus of carbon emissions, financial development, renewable energy consumption, and technological innovation: What should be the priorities in light of COP 21 Agreements?, J. Environ. Manage. 271 (2020) 111027. doi:10.1016/j.jenvman.2020.111027.

[40] S. Casanova, R. V. Silva, J. de Brito, M.F.C. Pereira, Mortars with alkali-activated municipal solid waste incinerator bottom ash and fine recycled aggregates, J. Clean. Prod. 289 (2021) 125707. doi:10.1016/j.jclepro.2020.125707.

[41] Z. Wang, S.M. Park, H.R. Khalid, H.K. Lee, Hydration properties of alkali-activated fly ash/slag binders modified by MgO with different reactivity, J. Build. Eng. (2021) 103252. doi:10.1016/j.jobe.2021.103252.

[42] J. He, W. Zheng, W. Bai, T. Hu, J. He, X. Song, Effect of reactive MgO on hydration and properties of alkali-activated slag pastes with different activators, Constr. Build. Mater. 271 (2021) 121608. doi:10.1016/j.conbuildmat.2020.121608.

[43] F. Jin, A. Al-Tabbaa, Strength and drying shrinkage of slag paste activated by sodium carbonate and reactive MgO, Constr. Build. Mater. 81 (2015) 58–65.

doi:10.1016/j.conbuildmat.2015.01.082.

[44] F. Jin, K. Gu, A. Al-Tabbaa, Strength and drying shrinkage of reactive MgO modified alkali-activated slag paste, Constr. Build. Mater. 51 (2014) 395–404. doi:10.1016/j.conbuildmat.2013.10.081.

[45] D.H. Vo, C.L. Hwang, M.D. Yehualaw, M.C. Liao, The influence of MgO addition on the performance of alkali-activated materials with slag−rice husk ash blending, J. Build. Eng. 33 (2021) 101605. doi:10.1016/j.jobe.2020.101605.

[46] X. Ke, Y. Duan, Coupling machine learning with thermodynamic modelling to develop a composition-property model for alkali-activated materials, Compos. Part B Eng. 216 (2021) 108801. doi:10.1016/j.compositesb.2021.108801.

[47] M.S.H. Khan, A. Castel, Effect of MgO and Na2SiO3 on the carbonation resistance of alkali activated slag concrete, Mag. Concr. Res. 70 (2018) 685–692. doi:10.1680/jmacr.17.00062.

[48] M. Ben Haha, B. Lothenbach, G. Le Saout, F. Winnefeld, Influence of slag chemistry on the hydration of alkali-activated blast-furnace slag - Part I: Effect of MgO, Cem. Concr. Res. 41 (2011) 955–963. doi:10.1016/j.cemconres.2011.05.002.

[49] S.M. Park, J.G. Jang, H.K. Lee, Unlocking the role of MgO in the carbonation of alkali-activated slag cement, Inorg. Chem. Front. 5 (2018) 1661–1670. doi:10.1039/c7qi00754j.

[50] Z. Wang, H.R. Khalid, S.M. Park, S.J. Bae, H.K. Lee, MgO-induced phase variation in alkali-activated binders synthesized under hydrothermal conditions,

Mater. Struct. Constr. 54 (2021) 1–18. doi:10.1617/s11527-021-01689-8.

[51] D.H. Vo, C.L. Hwang, K.D. Tran Thi, M.C. Liao, M.D. Yehualaw, Engineering performance of high-content MgO-Alkali-activated slag mortar incorporating fine recycled concrete aggregate and fly ash, J. Mater. Cycles Waste Manag. 23 (2021) 778–789. doi:10.1007/s10163-020-01171-7.

[52] J. He, X. Bu, W. Bai, W. Zheng, Q. Gao, Y. Wang, Preparation and properties of self-compacting alkali-activated slag repair mortar, Constr. Build. Mater. 252 (2020) 119034. doi:10.1016/j.conbuildmat.2020.119034.

[53] D. Zhang, Z. Ghouleh, Y. Shao, Review on carbonation curing of cement-based materials, J. CO2 Util. 21 (2017) 119–131. doi:10.1016/j.jcou.2017.07.003.

[54] C. Shi, F. He, Y. Wu, Effect of pre-conditioning on CO2 curing of lightweight concrete blocks mixtures, Constr. Build. Mater. 26 (2012) 257–267. doi:10.1016/j.conbuildmat.2011.06.020.

[55] D. Suescum-Morales, D. Cantador-Fernandez, J.M. Fernández, J.R. Jiménez, Potential CO2 capture in one-coat limestone mortar modified with Mg3Al–CO3 calcined hydrotalcites using ultrafast testing technique, Chem. Eng. J. 415 (2021). doi:10.1016/j.cej.2021.129077.

[56] C. Liang, B. Pan, Z. Ma, Z. He, Z. Duan, Utilization of CO2 curing to enhance the properties of recycled aggregate and prepared concrete: A review, Cem. Concr. Compos. 105 (2020) 103446. doi:10.1016/j.cemconcomp.2019.103446.

[57] S.K. Kaliyavaradhan, T.C. Ling, Potential of CO2 sequestration through construction and demolition (C&D) waste - An overview, J. CO2 Util. 20 (2017)

234–242. doi:10.1016/j.jcou.2017.05.014.

[58] B. Lu, C. Shi, J. Zheng, T.C. Ling, Carbon dioxide sequestration on recycled aggregates, Elsevier Ltd, 2018. doi:10.1016/B978-0-08-102444-7.00011-3.

[59] L. Quesada, M. del R. Perez, D. Fernández, A. Amores, J. maria Fernández, Optimum Particle Size of Treated Calcites for CO2 Capture in a Power Plant, (2019) 1–17.

[60] J. Zhang, C. Shi, Y. Li, X. Pan, C.S. Poon, Z. Xie, Performance enhancement of recycled concrete aggregates through carbonation, J. Mater. Civ. Eng. 27 (2015). doi:10.1061/(ASCE)MT.1943-5533.0001296.

[61] V. Rostami, Y. Shao, A.J. Boyd, Carbonation curing versus steam curing for precast concrete production, J. Mater. Civ. Eng. 24 (2012) 1221–1229. doi:10.1061/(ASCE)MT.1943-5533.0000462.

[62] B. Zhan, C.S. Poon, Q. Liu, S. Kou, C. Shi, Experimental study on CO2 curing for enhancement of recycled aggregate properties, Constr. Build. Mater. 67 (2014) 3–7. doi:10.1016/j.conbuildmat.2013.09.008.

[63] S.C. Kou, B.J. Zhan, C.S. Poon, Use of a CO2 curing step to improve the properties of concrete prepared with recycled aggregates, Cem. Concr. Compos. 45 (2014) 22–28. doi:10.1016/j.cemconcomp.2013.09.008.

[64] M. Nedeljković, B. Ghiassi, S. van der Laan, Z. Li, G. Ye, Effect of curing conditions on the pore solution and carbonation resistance of alkali-activated fly ash and slag pastes, Cem. Concr. Res. 116 (2019) 146–158. doi:10.1016/j.cemconres.2018.11.011.

[65] M. Sufian Badar, K. Kupwade-Patil, S.A. Bernal, J.L. Provis, E.N. Allouche, Corrosion of steel bars induced by accelerated carbonation in low and high calcium fly ash geopolymer concretes, Constr. Build. Mater. 61 (2014) 79–89. doi:10.1016/j.conbuildmat.2014.03.015.

[66] K. Pasupathy, M. Berndt, J. Sanjayan, P. Rajeev, D.S. Cheema, Durability Performance of Precast Fly Ash–Based Geopolymer Concrete under Atmospheric Exposure Conditions, J. Mater. Civ. Eng. 30 (2018) 04018007. doi:10.1061/(asce)mt.1943-5533.0002165.

[67] M. Babaee, M.S.H. Khan, A. Castel, Passivity of embedded reinforcement in carbonated low-calcium fly ash-based geopolymer concrete, Cem. Concr. Compos. 85 (2018) 32–43. doi:10.1016/j.cemconcomp.2017.10.001.

[68] M.S.H. Khan, A. Castel, A. Noushini, Carbonation of a low-calcium fly ash geopolymer concrete, Mag. Concr. Res. 69 (2017) 24–34. doi:10.1680/jmacr.15.00486.

[69] S. Liu, Y. Hao, G. Ma, Approaches to enhance the carbonation resistance of fly ash and slag based alkali-activated mortar- experimental evaluations, J. Clean. Prod. 280 (2021) 124321. doi:10.1016/j.jclepro.2020.124321.

[70] S.A. Bernal, J.L. Provis, B. Walkley, R. San Nicolas, J.D. Gehman, D.G. Brice, A.R. Kilcullen, P. Duxson, J.S.J. Van Deventer, Gel nanostructure in alkali-activated binders based on slag and fly ash, and effects of accelerated carbonation, Cem. Concr. Res. 53 (2013) 127–144. doi:10.1016/j.cemconres.2013.06.007.

[71] UNE-EN-13295, Products and systems for the protection and repair of concrete

structures. Test methods. Determination of resistance to carbonation, (2005).

[72] O. Burciaga-Dıaz, J. Iv an Escalante-Garc ıa, Structure, Mechanisms of Reaction, and Strength of an Alkali-Activated Blast-Furnace Slag, (2013). doi:10.1111/jace.12620.

[73] M. Ben Haha, G. Le Saout, F. Winnefeld, B. Lothenbach, Influence of activator type on hydration kinetics, hydrate assemblage and microstructural development of alkali activated blast-furnace slags, Cem. Concr. Res. 41 (2011) 301–310. doi:10.1016/j.cemconres.2010.11.016.

[74] S.A. Bernal, R. San Nicolas, R.J. Myers, R. Mejía De Gutiérrez, F. Puertas, J.S.J. Van Deventer, J.L. Provis, MgO content of slag controls phase evolution and structural changes induced by accelerated carbonation in alkali-activated binders, Cem. Concr. Res. 57 (2014) 33–43. doi:10.1016/j.cemconres.2013.12.003.

[75] H.N. Yoon, S.M. Park, H.K. Lee, Effect of MgO on chloride penetration resistance of alkali-activated binder, Constr. Build. Mater. 178 (2018) 584–592. doi:10.1016/j.conbuildmat.2018.05.156.

[76] E.R. McCaslin, C.E. White, A parametric study of accelerated carbonation in alkali-activated slag, Cem. Concr. Res. 145 (2021) 106454. doi:10.1016/j.cemconres.2021.106454.

[77] F. Cavani, F. Trifirò, A. Vaccari, Hydrotalcite-type anionic clays: Preparation, properties and applications., Catal. Today. 11 (1991) 173–301. doi:10.1016/0920-5861(91)80068-K.

[78] N.K. Lee, K.T. Koh, M.O. Kim, G.H. An, G.S. Ryu, Physicochemical changes

caused by reactive MgO in alkali-activated fly ash/slag blends under accelerated carbonation, Ceram. Int. 43 (2017) 12490–12496. doi:10.1016/j.ceramint.2017.06.119.

[79] C. Unluer, A. Al-Tabbaa, Impact of hydrated magnesium carbonate additives on the carbonation of reactive MgO cements, Cem. Concr. Res. 54 (2013) 87–97. doi:10.1016/j.cemconres.2013.08.009.

[80] ASTM-C618, Standard Specification for Coal Fly Ash and Raw or Calcined Natural Pozzolan for use in concrete, 2019.

[81] M. Nepomuceno, L. Oliveira, S.M.R. Lopes, Methodology for mix design of the mortar phase of self-compacting concrete using different mineral additions in binary blends of powders, Constr. Build. Mater. 26 (2012) 317–326. doi:10.1016/j.conbuildmat.2011.06.027.

[82] UNE-EN 196-1: 2018, Methods of testing cement. Part 1: Determination of strength, (2018).

[83] JCPDS, Joint Committee on Power Diffraction Standard-International Centre for Diffraction, 2003.

[84] EN-1015-6, Methods of test mortar for mansory. Part 6: Determination of bulk density of fresh mortar, (1999).

[85] EN-1015-3, Methods of test mortart masonry: Part 3: Determination of consistence of fresh mortar (by flow table), 2000.

[86] EN-1015-11, Methods of test for mortar for mansory. Part 11: Determination of flexural and compressive strenght of hardened mortar, (2000).

[87] UNE-EN 12504-4:2006, Testing concrete. Part 4: Determination of ultrasonic pulse velocity, (2006).

[88] U. American Society for Testing and Materials, West Conshohocken, Pennsylvania, ASTM-E1876, 2015, Standard Test Method for Dynamic Young's Modulus, Shear Modulus and Poisson's Ratio by Impulse Excitation of Vibration, 2015.

[89] UNE-EN-1015-13:1993, Methods of Test for Mortar for Masonry-Part 13: Determination of Dimensional Stability of Hardened Mortars, (1993).

[90] EN-1015-10, Methods of test mortar for mansory. Part 6: Determination of bulk density of hardened mortar, (2000).

[91] Parveen, D. Singhal, M.T. Junaid, B.B. Jindal, A. Mehta, Mechanical and microstructural properties of fly ash based geopolymer concrete incorporating alccofine at ambient curing, Constr. Build. Mater. 180 (2018) 298–307. doi:10.1016/j.conbuildmat.2018.05.286.

[92] D. Suescum-Morales, J.D. Ríos, A.M.- De La Concha, H. Cifuentes, J.R. Jiménez, J.M. Fernández, Effect of moderate temperatures on compressive strength of ultra-high-performance concrete: A microstructural analysis, Cem. Concr. Res. 140 (2021) 106303. doi:10.1016/j.cemconres.2020.106303.

[93] T. Gonçalves, R. V. Silva, J. de Brito, J.M. Fernández, A.R. Esquinas, Mechanical and durability performance of mortars with fine recycled concrete aggregates and reactive magnesium oxide as partial cement replacement, Cem. Concr. Compos. 105 (2020) 1–10. doi:10.1016/j.cemconcomp.2019.103420.

[94] UNE-EN 450-1, Fly ash for concrete. Pat 1: Definition, specifications and conformity criteria, (2013).

[95] E. Ul Haq, S. Kunjalukkal Padmanabhan, A. Licciulli, Synthesis and characteristics of fly ash and bottom ash based geopolymers-A comparative study, Ceram. Int. 40 (2014) 2965–2971. doi:10.1016/j.ceramint.2013.10.012.

[96] I.N. Murthy, J.B. Rao, Investigations on Physical and Chemical Properties of High Silica Sand, Fe-Cr Slag and Blast Furnace Slag for Foundry Applications, Procedia Environ. Sci. 35 (2016) 583–596. doi:10.1016/j.proenv.2016.07.045.

[97] H. Meradi, L. Atoui, L. Bahloul, K. Boubendira, A. Bouazdia, F. Ismail, Characterization by Thermal Analysis of Natural Kieselguhr and Sand for Industrial Application, Energy Procedia. 74 (2015) 1282–1288. doi:10.1016/j.egypro.2015.07.773.

[98] S.A. Osseni, M. Masseguin, E. V. Sagbo, D. Neumeyer, J.Y. Kinlehounme, M. Verelst, R. Mauricot, Physico-chemical Characterization of Siliceous Sands from Houéyogbé in Benin Republic (West Africa): Potentialities of Use in Glass Industry, Silicon. (2018) 2015–2023. doi:10.1007/s12633-018-0022-y.

[99] C.L. Hwang, D.H. Vo, V.A. Tran, M.D. Yehualaw, Effect of high MgO content on the performance of alkali-activated fine slag under water and air curing conditions, Constr. Build. Mater. 186 (2018) 503–513. doi:10.1016/j.conbuildmat.2018.07.129.

[100] M. Dong, M. Elchalakani, A. Karrech, Curing Conditions of Alkali-Activated Fly Ash and Slag Mortar, J. Mater. Civ. Eng. 32 (2020) 04020122. doi:10.1061/(asce)mt.1943-5533.0003233.

[101] M.H. Samarakoon, P.G. Ranjith, F. Xiao, B.L. Avanthi Isaka, S.M. Gajanayake, Carbonation-induced properties of alkali-activated cement exposed to saturated and supercritical CO2, Int. J. Greenh. Gas Control. 110 (2021) 103429. doi:10.1016/j.ijggc.2021.103429.

[102] Z. LI, S. LI, Carbonation resistance of fly ash and blast furnace slag based geopolymer concrete, Constr. Build. Mater. 163 (2018) 668–680. doi:10.1016/j.conbuildmat.2017.12.127.

[103] H. Hafez, D. Kassim, R. Kurda, R.V. Silva, J. de Brito, Assessing the sustainability potential of alkali-activated concrete from electric arc furnace slag using the ECO2 framework, Constr. Build. Mater. 281 (2021) 122559. doi:10.1016/j.conbuildmat.2021.122559.

[104] A. Islam, U.J. Alengaram, M.Z. Jumaat, I.I. Bashar, S.M.A. Kabir, Engineering properties and carbon footprint of ground granulated blast-furnace slag-palm oil fuel ash-based structural geopolymer concrete, Constr. Build. Mater. 101 (2015) 503–521. doi:10.1016/j.conbuildmat.2015.10.026.

[105] I.A.E. Agency, Guide Book on Non-Destructive Testing of mortar structures. Training Curses Series nº 17, Vienna, Austria, 2002.

[106] H. Alanazi, J. Hu, Y.R. Kim, Effect of slag, silica fume, and metakaolin on properties and performance of alkali-activated fly ash cured at ambient temperature, Constr. Build. Mater. 197 (2019) 747–756. doi:10.1016/j.conbuildmat.2018.11.172.

[107] F. Jin, K. Gu, A. Al-Tabbaa, Strength and hydration properties of reactive MgO-activated ground granulated blastfurnace slag paste, Cem. Concr. Compos. 57

(2015) 8–16. doi:10.1016/j.cemconcomp.2014.10.007.

[108] Y. Fang, J. Liu, Y. Chen, Effect of magnesia on properties and microstructure of alkali-activated slag cement, Water Sci. Eng. 4 (2011) 463–469. doi:10.3882/j.issn.1674-2370.2011.04.010.

[109] Y. Fang, Y. Gu, Q. Kang, Effect of fly ash, MgO and curing solution on the chemical shrinkage of alkali-activated slag cement, Adv. Mater. Res. 168–170 (2011) 2008–2012. doi:10.4028/www.scientific.net/AMR.168-170.2008.

[110] K. Mei, T. Gu, Y. Zheng, L. Zhang, F. Zhao, P. Gong, S. Huang, C. Zhang, X. Cheng, Effectiveness and microstructure change of alkali-activated materials during accelerated carbonation curing, Constr. Build. Mater. 274 (2021) 122063. doi:10.1016/j.conbuildmat.2020.122063.

[111] S. Chakraborty, B.W. Jo, Aqueous-based carbon dioxide sequestration, Elsevier Ltd, 2018. doi:10.1016/B978-0-08-102444-7.00003-4.

[112] S. Ruan, G. Kastiukas, S. Liang, X. Zhou, Influence of Early Oven Curing on the Alkali Activated Binders with Reactive Magnesia Replacement, KnE Eng. 2020 (2020) 207–214. doi:10.18502/keg.v5i4.6811.

[113] S. Charkhtab Moghaddam, R. Madandoust, M. Jamshidi, I.M. Nikbin, Mechanical properties of fly ash-based geopolymer concrete with crumb rubber and steel fiber under ambient and sulfuric acid conditions, Constr. Build. Mater. 281 (2021) 122571. doi:10.1016/j.conbuildmat.2021.122571.

[114] C. Luan, X. Shi, K. Zhang, N. Utashev, F. Yang, J. Dai, Q. Wang, A mix design method of fly ash geopolymer concrete based on factors analysis, Constr. Build.

Mater. 272 (2021) 121612. doi:10.1016/j.conbuildmat.2020.121612.

[115] E. Ul Haq, S.K. Padmanabhan, A. Licciulli, In-situ carbonation of alkali activated fly ash geopolymer, Constr. Build. Mater. 66 (2014) 781–786. doi:10.1016/j.conbuildmat.2014.06.012.

[116] V. Ferrini, C. De Vito, S. Mignardi, Synthesis of nesquehonite by reaction of gaseous CO2 with Mg chloride solution: Its potential role in the sequestration of carbon dioxide, J. Hazard. Mater. 168 (2009) 832–837. doi:10.1016/j.jhazmat.2009.02.103.

[117] C. Unluer, A. Al-Tabbaa, Green Construction with carbonating reactive magnesia porous blocks: effect of cement and water contents, Proc 2nd Int. Conf. Futur. Concr. (2011) 1–11.

Caption of illustrations

Figure 1 - Summary of the sample preparation process (A) and (B); (B) two different curing environments

Figure 2 - XRD patterns for fly ash (FA), fine sand (FS), coarse sand (CS) and MgO

Figure 3 - The particle size distributions of FA and MgO

Figure 4 - TGA (solid lines) and DTA (dotted lines) for FA, FS, CS and MgO

Figure 5 - SEM images and EDS mapping for (A) FA and (B) MgO

Figure 6 - Consistence and fresh density

Figure 7 - Compressive strength development of M0, M10 and M20 under EC and CC at the ages of 7, 14 and 28 days

Figure 8 - Flexural strength development of M0, M10 and M20 under EC and CC at the ages of 7, 14 and 28 days

Figure 9 - Ultrasonic pulse velocity (UPV) of M0, M10 and M20 under EC and CC at the ages of 7, 14 and 28 days

Figure 10 - Dynamic Young's modulus of M0, M10 and M20 under EC and CC at the ages of 7, 14 and 28 days

Figure 11 - Dimensional variation of M0, M10 and M20 under EC and CC at the ages of 7, 14 and 28 days

Figure 12 - Dry bulk density and accessible porosity for water of M0, M10 and M20 under EC and CC at the ages of 28 days

Figure 13 - Carbonation depth of M1, M2 and M3 under EC and CO_2-C at the ages of 7, 14 and 28 days

Figure 14 - XRD patterns of M0, M10 and M20 under EC and CC at the ages of 7 days

Figure 15 - XRD patterns of M0, M10 and M20 under EC and CC at the ages of 14 days

Figure 16 - XRD patterns of M0, M10 and M20 under EC and CC at the ages of 28 days

Figure 17 - TGA (solid lines) and DTA (dotted lines) of M0, M10 and M20 under EC and CC at the ages of 7 days

Figure 18 - TGA (solid lines) and DTA (dotted lines) of M0, M10 and M20 under EC and CC at the ages of 14 days

Figure 19 - TGA (solid lines) and DTA (dotted lines) of M0, M10 and M20 under EC and CC at the ages of 28 days

Figure 20 - SEM images and EDS of M0-EC-28 days.Mapping with the identification of the elements Si, Al, Ca, Na, C, K and Fe.

Figure 21 - SEM images of M0-CC-28 days.Mapping with the identification of the elements Si, Al, Ca, Na, C, K and Fe.

Figure 22 - SEM images of M20-EC-28 days with the identification of micro-cracks, unreacted fly ash and rounded growth.Mapping with the identification of the elements Si, Al, Ca, Na, C, K, Fe and MgO.

Figure 23 - SEM micrographs of M20-CC-28 days. Mapping with the identification of the elements Si, Al, Ca, Na, C, K , Fe and MgO.